Theses and Dissertations   Student Graduate Works

3-21-2013

Development of a Spectropolarimetric Capability

Evan J. Carlson

Follow this and additional works at: https://scholar.afit.edu/etd

Part of the Physics Commons

DEVELOPMENT OF A SPECTROPOLARIMETRIC REMOTE SENSING CAPABILITY

THESIS

Evan J. Carlson, Captain, USAF

AFIT-ENP-13-M-05

DEPARTMENT OF THE AIR FORCE

AIR UNIVERSITY

AIR FORCE INSTITUTE OF TECHNOLOGY

Wright-Patterson Air Force Base, Ohio

DEVELOPMENT OF A SPECTROPOLARIMETRIC REMOTE SENSING
CAPABILITY

THESIS

Presented to the Faculty

Department of Engineering Physics

Graduate School of Engineering and Management

Air Force Institute of Technology

Air University

Air Education and Training Command

In Partial Fulfillment of the Requirements for the

Degree of Master of Science in Applied Physics

Evan J. Carlson, B.S.

Captain, USAF

March 2013

AFIT-ENP-13-M-05

DEVELOPMENT OF A SPECTROPOLARIMETRIC REMOTE SENSING
CAPABILITY

Approved:

_____   _12 - Mar - 2013_

Dr. Kevin Gross (Chairman)   Date

_____   _12 Mar 2013_

Dr. Michael Marciniak (Member)   Date

_____   _13 MAR 2013_

Dr. Daniel LeMaster (Member)   Date

Abstract

An infrared, spectrally-resolved polarimetric measurement capability was established within the Remote Sensing Group at the Air Force Institute of Technology. Measurements were made using a Bomem MR-254 Michelson-based spectro-radiometer coupled to a Thorlabs WP50H-B rotating wire-grid polarizer in a Zinc Selenide substrate (2-30 µm). The Fourier-transform spectrometer (FTS) covers the near- and mid-infrared (0.9-5.5 µm) using Indium Antimonide (InSb, 1800-12000 cm^{-1}) and Indium Gallium Arsenide (InGaAs, 6000-14000 cm^{-1}) detectors. Degree of linear polarization (DOLP) measurements were made of Pyrex glass and an optical-grade Aluminum mirror at incident angles between 20-70 deg. Both smooth and roughened Pyrex were studied, and surface roughness was characterized by a KLA Tencor profiler. A broadband integrating sphere was used as a light source. The spectro-polarimetric response of the FTS was determined assuming a temperature-insensitive gain and is described in the document. Reflected intensity measurements of the integrating sphere at polarizer angles of 0, 45, 90, and 135 deg were used to estimate the Stokes parameters S0, S1, & S2, and from them the DOLP. The material's complex index of refraction, surface roughness, and orientation affect the DOLP. Results of the DOLP measurements are compared to predictions based upon Fresnel's equations. Agreement was poor in some cases, and both the thermal stability of the FTS's polarimetric gain and the low polarizer extinction ratio above $\lambda = 2\mu m$ are partially responsible for these discrepancies. Benefits and limitations of this method are discussed, as well as suggestions for improvements to this technique.

Acknowledgments

I would like to thank my wife for her constant encouragement throughout this process. Her comfort has been an invaluable.

The AFIT experience has been a wonderful opportunity. The staff and fellow students have made it that way. My thesis advisor, Dr. Kevin Gross, has been an outstanding mentor. I've been very appreciative of his patients and motivating guidance throughout the past year. I wish him the best of luck in the future, and I hope this thesis lives up to his expectations. I would also like to extend my appreciation to Dr. Mathew Lange and Peter Borton for their assistance in conducting the material and surface characterization of the samples used in this work.

Evan Carlson

Table of Contents

List of Figures

List of Tables

List of Abbreviations

Imaging Fourier-transform Spectrometers	IFTS
Polarimatric Hyperspectral Imaging	PHSI
Fourier Transform Infrared	FTIR
Air Force Institute of Technology	AFIT
Hyperspectral Imagery	HSI
Degree of Linear Polarization	DOLP
Improvised Explosive Devices	IED
Infrared	IR
MODerate resolution atmospheric TRANsmission	MODTRAN
Digital Imaging and Remote Sensing Image Generation	DIRSIG
Bidirection Reflectance Distribution Function	BRDF
Long Wave Infrared	LWIR
Electromagnetic	EM
Meter Kilogram Second	MKS
Midwave Infrared	MWIR
Near Infrared	NIR
Optical Path Length Difference	OPLD
Analog to Digital Conversion	ADC
Zero Path Difference	ZPD
Direct Current	DC
Root Mean Squared	RMS

DEVELOPMENT OF A SPECTROPOLARIMETRIC REMOTE SENSING
CAPABILITY

I.   Introduction

It is my understanding that while the fields of both spectral and polarimetric measurements are mature and established, their concurrent measurement is uncommon and the simultaneous exploitation of both modalities has not been thoroughly explored. Fourier-transform spectrometers (FTS) have led to advances in capabilities that have allowed for more detailed remote sensing techniques to evolve. Equipping FTS with a wire grid polarizer allows for the ability to acquire polarimetric properties from an object. This combination adds the requirement to polarimetrically calibrate the instrument as well as radiometrically. The scope of this work is threefold: (1) to establish a new, spectro-polarimetric reflectance measurement capability at AFIT; (2) document best practices (learned through this effort) for accurate DOLP measurements; (3) demonstrate the current accuracy and limitations of the technique using smooth aluminum as well as smooth and roughened glass substrates. A method of interpreting the degree of linear polarization as a function of incident angle, surface roughness and wavelength is developed.

Research Approach

To accomplish the scope of work outlined, a theoretical understanding of the factors associated with spectropolarimetric measurements from a phenomena and instrumental

perspective is required. This work is the first phase of a larger effort to investigate the utility of polarimetric hyperspectral imagery for improved material identification and surface orientation determination. To gain experimental understanding of polarimetric measurements, data was collected with a Bomem 254 FTS combined with a Thorlabs ZeSe wire-grid infrared polarizer. Efforts were focused on developing a calibration method that would account for instabilities in the Bomem FTIR, as well as data processing to ensure that experimental results agreed with the predicted values. The experimental setup for taking measurements is uncomplicated; however, it was found that small errors in set up can result in large deviations from calculated values. Recommended improvements to the current experimental setup for measuring spectrally-resolved DOLP will be presented.

Document Structure

Chapter two of this document presents a review of the research related to this work. A brief historical perspective is provided along with an emphasis on instruments and techniques used to make spectral polarimetric measurements. Since this is a new capability at AFIT, with the potential for future research efforts, a detailed theoretical background is provided in chapter three. Included in chapter three will be technical details related to the equipment used for this research effort. Methodology, results, and analysis are addressed in chapter four of this document. Appendix A contains MATLAB code developed to generate the theoretical predictions as well as process the data collected. Each section of data will be given a description along with a reference to additional details.

II.   Literature Review

Historically, phenomena associated with the polarization of light have been observed since the 17th century and mathematically understood since the 19th century. Augustin-Jean Fresnel derived the mathematical treatment to describe the interaction between matter and light, and the equations he produced are used in models today [1]. He proved that light travels as a transverse wave and showed that light can become partially polarized by being reflected, emitted, or scattered. For example, depending on the incident angle, light reflected from glass or water can become completely polarized and light scatter in the sky can become partially polarized as well [23, 28]. Recent advances with spectrometers and infrared imagers have enabled the ability to exploit these polarimetric signals in a variety of applications from oceanography and military target detection, to material science [20, 21, 29]. For example, the combination of spectral and spatial content has been made with multispectral and hyperspectral technology. This review will discuss the previous work with spectral polarimetric measurements related to this research effort as well as the theoretical models necessary to provide useful applications.

Polarimetric Remote Sensing

Initial efforts to measure and quantify polarimetric signals from roughened surfaces were performed by Jordan and Lewis in the 1994 [2]. These experiments served as a good model for the research preformed in this thesis.   Their work focused on emission polarization of aluminum and glass in the long wave infrared that were heated above ambient temperatures. Using a rotatable linear polarizer and a quarter wave plate enabled making full Stokes vector measurements. Included in their measurements were

Gaussian distribution of surface slopes. By including this parameter, they showed how surface roughness decreases the DOLP from emitted radiation. More recent work performed by Gurtan and Dahmani also looked at the emission polarization from glass and included spectrally resolved measurements by using a FTIR spectrometer equipped with a wire-grid polarizer [5]. They extended the spectral range of the measurements and showed how the complex index of refraction, which is wavelength dependent for all materials, affects the DOLP. Their investigation also included measuring the DOLP as a function of wavelength of glass covered in Krylon and CARC paint, showing how different coatings alter the emitted DOLP. Both of these papers served as excellent sources for theoretical and experimental backgrounds for the work performed in this thesis.

Polarimetric Infrared Imaging

Applications of polarimetric imaging are broad but have particular use in military operational situations. Techniques developed by Pesses and Tan show that using DOLP images of satellites had the highest contrast when imaging a spinning spacecraft [30]. They went on to show how polarimetric rotation signatures can improve space object identification, and they applied their polarimetric methods to show how re-entry vehicle identification can be improved. Polarimetric measurements also have uses in terrestrial measurements as well. For example, surface landmine detection was investigated by Forssell in 2001 [21]. This work showed that DOLP measurements provided higher contrast for optical detection of mines. Others have investigated the application of these signals in detecting buried improvised explosive devices (IEDs) by measuring the

difference in reflected and emitted polarization from disturbed soils [21]. Also, from aerial platforms, the detection of military vehicles that were located in shaded area or covered by vegetation [16]. One potential application of polarimetric imaging is for use in the assistance of remote detection of nuclear materials. This research effort is primarily focused on the spectral nature of the DOLP.

Polarimetric Modeling

Surface roughness, incident angle, and material properties all affect polarimetric properties. For example, materials that are man-made generally have smoother surfaces than objects created in nature. This distinction allows for infrared (IR) imagers equipped with a polarization analyzer to distinguish between targets from a background even if they are camouflaged [16]. However, modeling how these signals propagate in an operational setting can be challenging when including the dynamic parameters involved in radiometric transfer. Algorithms have been generated to process these signals more efficiently for military uses [31,32]. Atmospheric models, such as MODTRAN, have incorporated polarimetric models to include the polarized radiation from the sky. The Air Force has developed a polarimetric atmospheric model (MODTRAN-P) to simulate atmospheric effects [33]. The Digital Imaging and Remote Sensing Image Generation Model (DIRSIG), created by the Rochester Institute of Technology, is a model based on first principles that generates synthetic images. The DIRSIG model simulates a wide variety of phenomena for sensor modeling, among an assortment of other uses [35]. Critical for modeling the spectral and polarimetric signatures of targets in any environment requires detailed understanding about how materials emit and reflect

different parts of the electromagnetic spectrum. Polarized bidirectional reflectance distribution functions (pBRDF) extend the BRDF model by incorporating a statistical distribution of surface parameters. This model can be applied in either the reflective and emissive spectral regions and are related by Kirchoff's law

$$\varepsilon = 1 - r, \tag{2-1}$$

which applies for surfaces in thermal equilibrium for opaque materials, where ε and r are the emissivity and reflectivity of the material of interest [13, 15, 25]. BRDF models quantitatively characterize the directional scatter of an object, and these objects can be classified into two broad categories, diffuse and specular [4]. Accurate models are vital for determining the physical limitations of the instruments used and to produce valuable data.

Spectropolarimetric Instruments

Passive remote sensing techniques have been used to exploit polarimetric signals for target detection in a variety of environments. A common method to obtain spectral information is with the use of a Michelson interferometer; this technology is mature and well developed. The combination of these two capabilities is known as spectropolarimetry, which enables the ability to measure a material or target's polarization properties as functions of wavelength [17]. Infrared imaging has also been used to investigate polarized emission and reflectance properties of materials and targets of interest [35]. Large amounts of data are produced while collecting spectropolarimetric data. Improvements in data reduction methods and processing algorithms to handle the

large amounts of data has allowed for better signal processing. Employment of a formal mathematical treatment of processing polarimetric measurements using Mueller matrices has been investigated since the 1970's. Efforts made by D. H. Goldstein, R. A. Chipman, and D. B. Chenault have produced Fourier analysis, error reduction analysis and data reduction methods to improve the accuracy and efficiency of infrared spectropolarimetric methods [14]. These methods are analyzed and incorporated into this research effort.

Several instruments have been used to take advantage of the information content contained in polarimetric and spectral signals. For example, microbolometers can be equipped with polarizers to enable the ability to measure all Stokes parameters simultaneously; minimizing temporal changes in polarized signals [36]. Multiple spectrometers have been built for airborne and space platforms. For example, Geosynchronous Imaging Fourier Transform Spectrometer (GIFTS) is a space asset located in geosynchronous orbit at 40,000 km [16]. This satellite operates in the MWIR (4.4 to 6.1 microns) and LWIR (8.8 to 14.5 microns) and collects atmospheric data. The first Fourier Transform Hyperspectral Imager (FTHSI) sensor was developed by NASA to cover the NIR spectral range [16]. This technology has been further developed. AFIT owns two field portable imaging radiometric spectrometers built by Telops Inc. that were primarily designed for remote chemical sensing applications [37]. These instruments are based on a Michelson interferometer and operate in the LWIR and MWIR. The LWIR system has been upgraded with a rotatable wire grid polarizer to enable PHSI measurements. This capability could potentially unlock new areas of application.

III. Electromagnetic Theory and Application

Introduction

In this chapter, the interaction of electromagnetic (EM) waves with materials will be addressed. First, the mathematical principles for describing an EM wave as well as the properties of materials that affect phenomena for remote sensing will be presented. The derivations presented can be found in most optics textbooks [1].   In addition, a brief theory of operation for Fourier transform spectrometers will be discussed since that is the instrument used for this work.   In particular, the topics that proved most useful in understanding the instrument's role will be addressed.

Electromagnetic Waves

Remote sensing is the process of extracting information from a scene without coming into contact with the objects in that scene. This is performed typically by collecting emitted or reflected light from objects.   In order to obtain meaningful information, understanding how light or electromagnetic waves behave is critical.   Maxwell's equations fully describe the interaction between electric and magnetic fields as well as their interaction with charged matter. When no charges are present, the wave equation for propagation in free space can be derived from Maxwell's equations.

$$\nabla^2 \boldsymbol{E} = \frac{1}{c^2} \frac{\partial^2 \boldsymbol{E}}{\partial^2 t^2} \tag{3-1}$$

Solutions to the wave equation come in the form of a plane wave described by

$$\vec{E}(r,t) = E_0 e^{-i(\vec{k}\cdot\vec{r} - \omega t)}, \tag{3-2}$$

where E_0 is the amplitude, $\vec{k}$ is the wave vector equal to $2\pi/\lambda$ where λ is the wavelength of light, and ω is the frequency of oscillation. The solutions for the magnetic wave are identical in form to the electric field and the two quantities are related by

$$B_0 = \frac{E_0}{v} = \frac{nE_0}{c_0}, \tag{3-2}$$

where c_0 is the speed of light in free space.

In vacuum, the wave travels unattenuated in a straight line at speed c_0. However, when encountering a material, the wave can be attenuated, and its speed and direction can change as well. These effects can be quantified if the material's complex index of refraction $\tilde{n}$ is known, and it is given by

$$\tilde{n} = n + i\kappa, \tag{3-3}$$

where n is the real and κ is the imaginary part of the refractive index. The real part governs the change in speed and the imaginary part is responsible for how EM energy is absorbed by the material. For dielectric materials, the imaginary part is nearly zero. The imaginary part of the index of refraction is related to the conductivity of the material by

$$\tilde{n} = \sqrt{1 + i\left(\frac{\sigma}{\varepsilon_0 \omega}\right)} = n + i\kappa, \tag{3-4}$$

where σ is the conductivity of the material, ε_0 is the permittivity of free space and is equal to 8.85 x 10^{-12} $[\frac{c^2}{N\cdot m^2}]$ in mks units. This expression can be incorporated into the wave vector $\vec{k}$ which yields how the plane wave will propagate in the material with a given conductivity.

$$\vec{k} = 2\pi/(\lambda/\tilde{n}) = (n + i\kappa)\,{}^{\omega}\!/_{c}\,. \tag{3-5}$$

Inserting this expression for the complex index of refraction into the solution for the wave equation for the electric field we get

$$\vec{E_i} = E_{0i}e^{-i(\vec{k_i}\cdot\vec{r}-\omega t)} \tag{3-6}$$

$$\vec{E_i} = E_{0i}e^{-i((n+i\kappa)\frac{\omega}{c}\cdot\vec{r}-\omega t)} \tag{3-7}$$

$$\vec{E_i} = E_{0i}e^{-i\omega(\frac{n}{c}\cdot\vec{r}-t)}e^{-\omega(\frac{\kappa}{c}\cdot\vec{r})}. \tag{3-8}$$

The first exponential of equation (3-8) represents the oscillatory electric field associated with a traveling wave of light. The second exponential of equation (3-8) is a negative exponential, indicating that the energy in the wave is being absorbed by the material in which it is propagating. Typically, metals are the materials that have significant complex part of the index of refraction; for this reason metals are not transparent. Figure 1 is an example of the index of refraction for Aluminum.
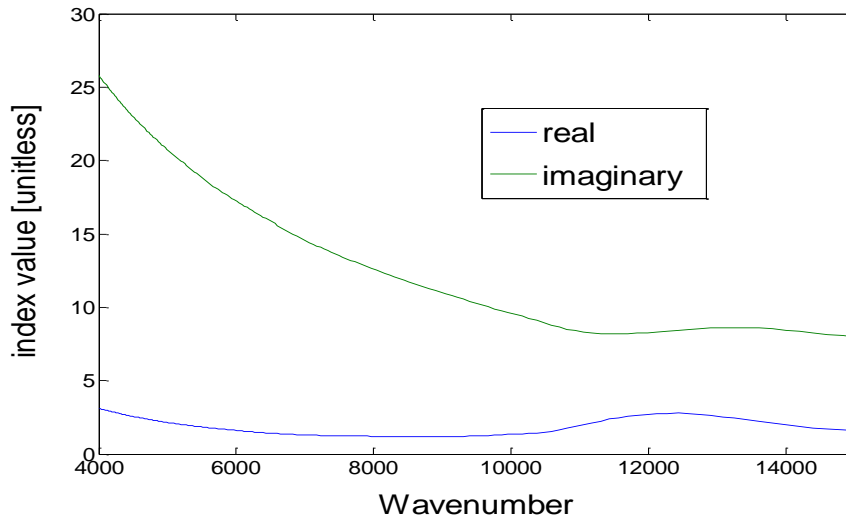
Figure 1. Showing the wavelength dependence of the complex index of refraction of Aluminum [27].

Glass, which is a dielectric, has an imaginary component which is near zero in the visible part of the spectrum. A functional form for the index of refraction, known as the dispersion relationship, can be obtained based on the Sellmeir equation which is an empirical relation between the refractive index and wavelength for a particular transparent medium [1]. The form for most glasses is

$$n^2(\lambda) = 1 + \frac{B_1\lambda^2}{\lambda^2 - C_1} + \frac{B_2\lambda^2}{\lambda^2 - C_2} + \frac{B_3\lambda^2}{\lambda^2 - C_3} \tag{3-9}$$

Where λ is the wavelength in microns, n is the refractive index, $B_{1,2,3}$ and $C_{1,2,3}$ are experimentally determined coefficients. Figure 2 shows the refractive index for Pyrex, a common glass that was used in this work. Figure 3 shows measured index of refraction for Pyrex showing the limitations of this equation in the LWIR where the imaginary component plays a significant roll.
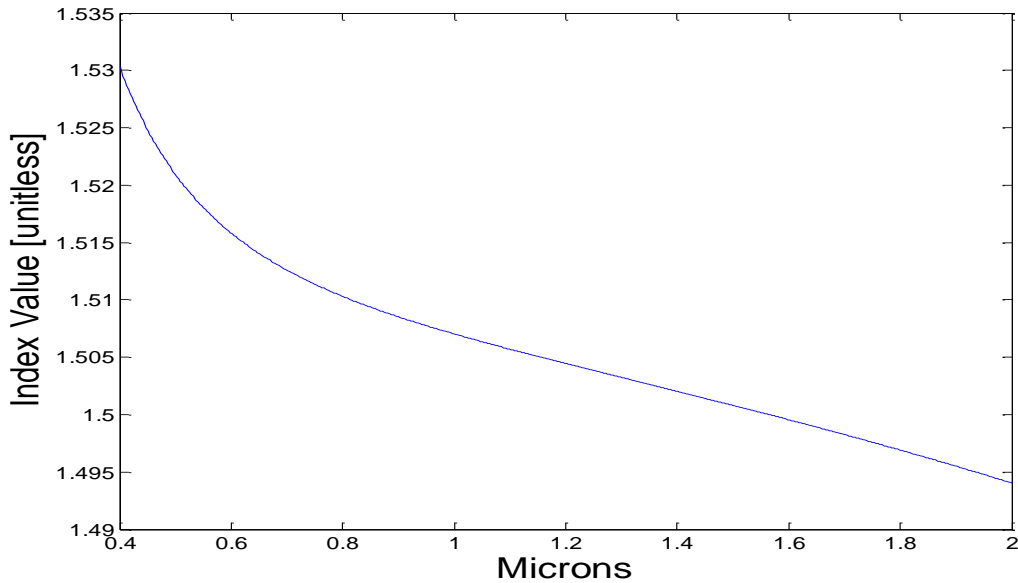
Figure 2. Showing the wavelength dependence of Pyrex, a common glass. This material is a dielectric and the complex part of the index of refraction is negligible. The functional form is based on the dispersion formula [27] which applies only in the visible and NIR.
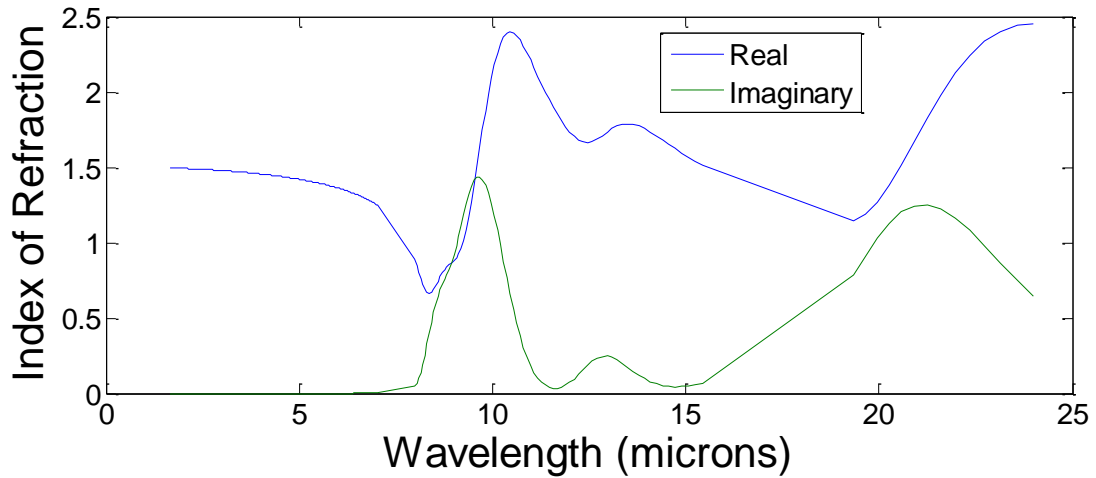
Figure 3: Measured index of refraction of Pyrex samples used for this research. In the long wave IR, Pyrex becomes absorbent indicated by the imaginary component.

Oscillations of the electric field for a beam of light are on the order of 10^{14} Hz and therefore are too fast to detect an individual oscillation. What is measurable is the time averaged electric field squared. Several units of measurement have been adopted to quantify electromagnetic radiation. Table 1 describes the units involved [16].

Table 1: Radiometry Terminology

Quantity	Designation	Relationship	Units
Irradiance	E	$E = \dfrac{\partial P}{\partial A} = \int E_\lambda \partial \lambda$	$\mu W / cm^2$
Spectral Irradiance	E_λ	$E_\lambda = \dfrac{\partial P}{\partial A \partial \lambda} = \int L_\lambda \partial \Omega$	$\mu W / cm^2\ \mu m$
Radiance	L	$L = \dfrac{\partial P}{\partial A \partial \Omega} = \int L_\lambda \partial \lambda$	$\mu W / cm^2\ sr$
Spectral Radiance	L_λ	$L_\lambda = \dfrac{\partial P}{\partial A \partial \Omega \partial \lambda}$	$\mu W / cm^2\ \mu m\ sr$

Intensity	I	$I = \dfrac{\partial P}{\partial \Omega} = \displaystyle\int L \, dA$	$\mu W /_{sr}$
Power	P	$P = \displaystyle\int E \, dA = \int I \, d\Omega$	μW

The irradiance of an electromagnetic wave is given by the electric field amplitude squared per unit of area. By taking the complex conjugate of equation (3-8), the first exponential cancels, and we are left with

$$I = EE^* = E_0 E_0^* e^{-\frac{2\kappa(\omega \cdot z)}{c}} = I_0 e^{-\alpha(k \cdot z)}, \qquad (3\text{-}10)$$

which is known as Beer's law. The absorption coefficient is now defined to be $\alpha = \dfrac{2\kappa}{c} = \dfrac{4\pi\kappa}{\lambda}$ which indicates how EM waves of a certain frequency are absorbed.

When the light impinges on a surface, it must be either transmitted given by τ, reflected ρ, or absorbed α; this relation is given by

$$\rho + \alpha + \tau = 1, \qquad (3\text{-}11)$$

indicating that energy is conserved. Absorption has been discussed relating the conductivity of a material to how electromagnetic radiation interacts with that matter. When a material reaches steady state, absorption and emission are equal. If a material's transmission is zero, the relationship simplifies to

$$\rho + \varepsilon = 1, \qquad (3\text{-}12)$$

where ε is the emissivity of the material. Emission from materials is temperature dependent and follows Planck's Law.

Fresnel's Equations

In the NIR to MWIR, remote sensing is dominated by reflected light during the day, and in the LWIR emitted light dominates. Most operational techniques use the sun's light as a source which is naturally unpolarized. This light gets reflected by objects and therefore motivates the need to have equations describing how light is reflected from targets of interest. By solving the electromagnetic wave equations while imposing the condition that the waves must be continuous at all times, Fresnel's equations are derived. Coefficients for the reflected and transmitted amplitudes are obtained; these coefficients are functions of the complex index of refraction, and the incident angle relative to the surface normal. These are not to be confused with the reflectivity and transmissivity of a material which are the coefficients squared. The form of the wave equations stays the same while the wave vector, $\vec{k}$,changes.

$$\text{Incident Wave: } \vec{E_i} = E_{0i}e^{-i(\vec{k_i}\cdot\vec{r}-\omega t)} \tag{3-13}$$

$$\text{Reflected Beam: } \vec{E_r} = E_{0r}e^{-i(\vec{k_r}\cdot\vec{r}-\omega t)} \tag{3-14}$$

$$\text{Transmitted Beam: } \vec{E_t} = E_{0t}e^{-i(\vec{k_t}\cdot\vec{r}-\omega t)} \tag{3-15}$$

$$\text{Where } |\vec{k_i}| = n_1 * k_0 \tag{3-16}$$

$$|\vec{k_r}| = n_1 * k_0 \tag{3-17}$$

$$|\vec{k_t}| = n_2 * k_0 \tag{3-18}$$
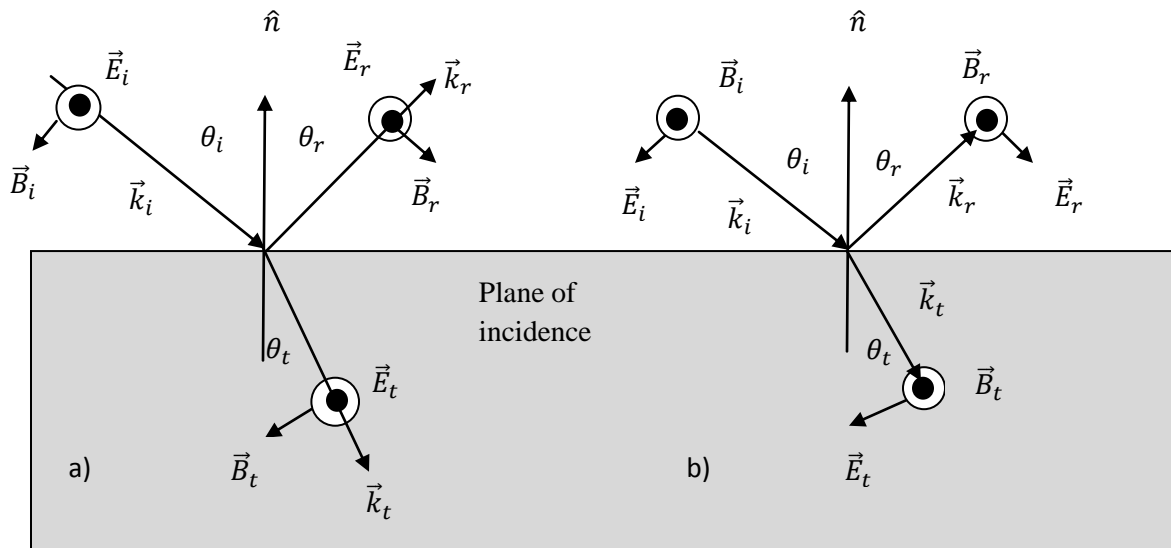
Figure 4. Incident plane wave with electric field oriented a) parallel to the plane of incidence and b) perpendicular to the plane of the incidence.

To illustrate this affect, figure 4(a) shows how electric field vectors oscillating perpendicular to the plane of incidence, represented by the circles, are reflected and transmitted. In figure 4(b), the electric field vectors are now oscillating parallel with the plane of incidence, and represented by the vector arrows where the magnetic field vectors are now represented by the circles. The wave vector k propagates perpendicularly to the oscillations of both the electric and magnetic fields.

To derive the reflective coefficients, two conditions must now be applied: first, that the waves must be continuous at the material interface and second, all waves must exist simultaneously. This indicates that the tangential component of electric field vector must be equal on either side of the interface. For any time t, this condition must be met and can be described by the equation

$$\hat{n} \times \vec{E_i} + \hat{n} \times \vec{E_r} = \hat{n} \times \vec{E_t}, \qquad (3\text{-}19)$$

where $\hat{n}$ is the unit vector normal to the plane of incidence. The only way that this can be true over the entire interface, and for all time, is if the arguments of the exponentials in equations (3-11), (3-12), and (3-13) meet the following condition,

$$\left(\vec{k_i} \cdot \vec{z} - \omega_i t\right) = \left(\vec{k_r} \cdot \vec{z} - \omega_r t\right) = \left(\vec{k_t} \cdot \vec{z} - \omega_t t\right). \qquad (3\text{-}20)$$

Equation (3-18) indicates that the phase of each component must be matched at the boundary. For any time t, and at the point of intersection, $z = 0$,

$$\omega_i = \omega_t = \omega_r \qquad (3\text{-}21)$$

This shows that the frequency does not change at the interface. Addressing the wave vectors at time equal to zero,

$$\vec{k_i} \cdot \vec{z} = \vec{k_r} \cdot \vec{z} = \vec{k_t} \cdot \vec{z}. \qquad (3\text{-}22)$$

From this equation, we can look at the relationship between the incident and reflected wave vectors.

$$\vec{k_i} \cdot \vec{z} = \vec{k_r} \cdot \vec{z} \qquad (3\text{-}23)$$

Since the dot product of any two vectors is $\vec{a} \cdot \vec{b} = |a||b| \cos\theta$, and the wave vectors are equal in magnitude, the law of reflection is derived.

$$\sin\theta_i = \sin\theta_r \quad \text{or} \quad \theta_i = \theta_r \qquad (3\text{-}24)$$

Now looking at the incident and transmitted beams:

$$\vec{k_i} \cdot \vec{z} = \vec{k_t} \cdot \vec{z} \qquad (3\text{-}25)$$

In this situation, $\vec{k_i}$ does not equal $\vec{k_t}$ due to the change in refractive index.

$$\vec{k_t} = \frac{n_2 \omega}{c} \text{ and } \vec{k_i} = \frac{n_1 \omega}{c} \qquad (3\text{-}26)$$

Substituting this expression into the previous equations yields Snell's Law:

$$n_1 * \sin \theta_i = n_2 * \sin \theta_t. \qquad (3\text{-}27)$$

The orientation of the incident electric field vectors impacts the coefficients that are reflected and transmitted. These principles also apply to the oscillating magnetic vectors associated with the electromagnetic wave. Two treatments are required to fully describe the interaction. This is performed by separating the electric and magnetic field vectors into the x and y components or perpendicular and parallel components to the plane of incidence. These are also known as s polarization for electric field vectors oscillating parallel to the plane of incidence and p polarization for vectors oscillating perpendicular to the plane of incidence .

For the perpendicular condition

$$E_i + E_r = E_t \qquad (3\text{-}28)$$

$$B_i \cos \theta_i - B_r \cos \theta_r = B_t \cos \theta_t. \qquad (3\text{-}29)$$

The implication from the above equations is that the tangential components of E and B are equal on both sides of the interface. For the perpendicular condition

$$-B_i + B_r = -B_t \qquad (3\text{-}30)$$

$$E_i \cos \theta_i - E_r \cos \theta_r = E_t \cos \theta_t \qquad (3\text{-}31)$$

These equations for electric and magnetic fields are transformed by the relationship

$$E = vB = \left(\frac{c}{n}\right) B \quad or \quad B = \frac{nE}{c} \qquad (3\text{-}32)$$

This expression transforms the equations for the perpendicular case (3-26) and (3-27) into

$$E_i + E_r = E_t \tag{3-33}$$

$$n_1 E_i \cos \theta_i - n_1 E_r \cos \theta_r = n_2 E_t \cos \theta_t, \tag{3-34}$$

and transform equations (3-31) and (3-32) for the parallel

$$E_i \cos \theta_i - E_r \cos \theta_r = E_t \cos \theta_t \tag{3-35}$$

$$-n_1 E_i + n_1 E_r = -n_2 E_t. \tag{3-36}$$

By simply taking the ratio of the reflected and incident electric field vectors and eliminating the transmitted component, the reflection coefficients are obtained. These equations are for the:

$$\text{perpendicular case,} \quad r_{perp} = \frac{E_r}{E_i} = \frac{\cos \theta_i - n*\cos \theta_t}{\cos \theta_i + n*\cos \theta_t}, \tag{3-37}$$

$$\text{and for the parallel case: } r_{para} = \frac{E_r}{E_i} = \frac{-n*\cos \theta_i - \cos \theta_t}{n*\cos \theta_i + \cos \theta_t} \tag{3-38}$$

$$\text{where } n = \frac{n_2}{n_1}. \tag{3-39}$$

To eliminate the inconvenient θ_t term, from Snell's Law, we know that $\sin \theta_i = n * \sin \theta_t$ and from Euler's formula $\sin^2 \theta + \cos^2 \theta = 1$, we get

$$n * \cos \theta_t = n\sqrt{1 - \sin^2 \theta_t} = n\sqrt{1 - \frac{\sin^2 \theta_i}{n^2}} = \sqrt{n^2 - \sin^2 \theta_i}. \tag{3-40}$$

By using this substitution, the reflection coefficients are all functions of n and θ_i. Inserting this expression into equation (3-35) and (3-36) gives for the

$$\text{perpendicular case: } r_{perp} = \frac{E_r}{E_i} = \frac{\cos \theta_i - \sqrt{n^2 - \sin^2 \theta_i}}{\cos \theta_i + \sqrt{n^2 - \sin^2 \theta_i}}, \tag{3-41}$$

28

And parallel case: $r_{para} = \dfrac{E_r}{E_i} = \dfrac{-n^2 * \cos\theta_i + \sqrt{n^2 - \sin^2\theta_i}}{n^2 * \cos\theta_i + \sqrt{n^2 - \sin^2\theta_i}}$ \hfill (3-42)

Figure 5 shows these functions plotted versus the angle of incidence.
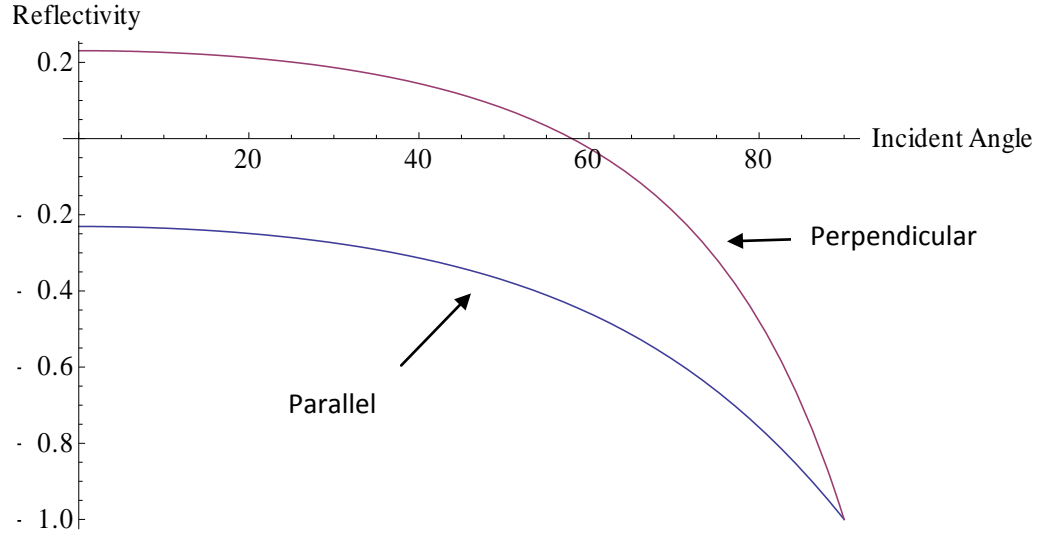
Figure 5. Reflection and coefficients versus incident angle of perpendicular and parallel components of the electric field for glass with an index of refraction = 1.5.

These ratios of the electric field amplitudes are not measureable quantities due to the rapid oscillation of the electric field vector. To define a measureable quantity, the Poynting vector, $\vec{S} = c^2 \epsilon_0 \vec{E} \times \vec{B}$, which defines the power per unit area in vacuum whose normal is parallel to $\vec{S}$, needs to be incorporated [1]. In addition, the time average of the Poynting vector gives irradiance or the radiant flux density (W/m^2). Also, the ratio of two radiant flux densities is defined to be reflectance, denoted by R, or transmittance denoted by T.

$$R \equiv \frac{I_r A \cos\theta_r}{I_i A \cos\theta_i} = \frac{I_r}{I_i} \text{ and } T \equiv \frac{I_r \cos\theta_t}{I_i \cos\theta_i}. \hfill (3-43)$$

Relating the reflectance to reflectivity requires using the Poynting vector. Since $B = \frac{nE}{c}$, $\vec{S}$ reduces to

$$\langle \vec{S} \rangle = \frac{c\epsilon_0}{2} E_0^2 = I, \tag{3-44}$$

$$R = \left(\frac{E_{0r}}{E_{0i}}\right)^2 = r^2. \tag{3-45}$$

Figure 6 illustrates how the reflectance of glass depends upon the incident angle. Around 55 degrees, the parallel component reaches zero. As a result, reflected light will be completely polarized.
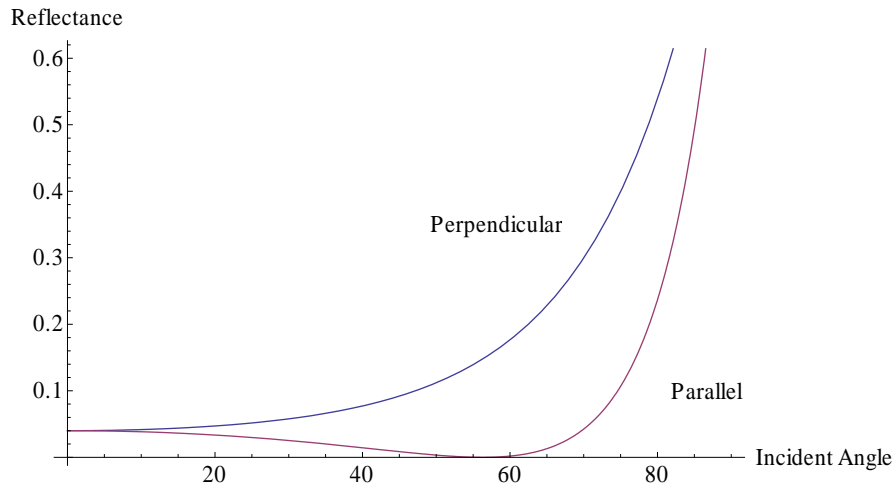
Figure 6. Reflectance values for perpendicular and parallel components of the electric field versus incident angle.

For material in the limit where the complex part of the index of refraction is zero, these equations hold true. However, when the complex part cannot be ignored, typically for metals, these equations need slight modification. Inserting the expression for the complex index of refraction, equation (3-4), into the solution for the wave equation for the electric field we get: for the perpendicular component of the electric field vector,

$$r = \frac{E_r}{E_i} = \frac{\cos\theta - \sqrt{(n_R^2 - n_I^2 - \sin^2\theta_i) + i(2n_R n_I)}}{\cos\theta + \sqrt{(n_R^2 - n_I^2 - \sin^2\theta_i) + i(2n_R n_I)}} \qquad (3\text{-}46)$$

and for the parallel component of the electric field vector,

$$r = \frac{E_r}{E_i} = \frac{-[(n_R^2 - n_I^2) + i(2n_R n_I)]\cos\theta - \sqrt{(n_R^2 - n_I^2 - \sin^2\theta_i) + i(2n_R n_I)}}{[(n_R^2 - n_I^2) + i(2n_R n_I)]\cos\theta + \sqrt{(n_R^2 - n_I^2 - \sin^2\theta_i) + i(2n_R n_I)}}. \qquad (3\text{-}47)$$

Figure 7 shows the spectral dependence of Aluminum for an angle of incidence of 80 degrees. Aluminum is highly reflective across a wide spectral range for both perpendicular and parallel components. To get a significant difference between the two components, large incident angles are necessary.
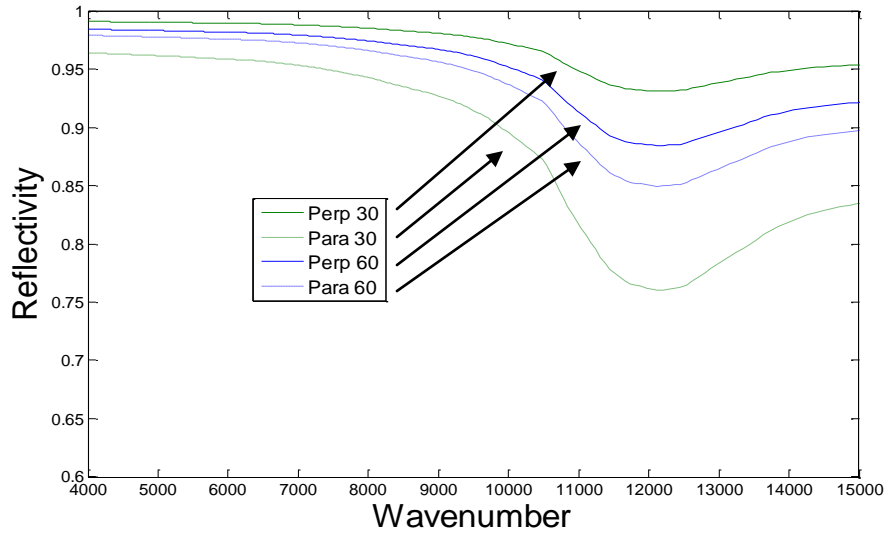
Figure 7. Parallel and perpendicular components reflected at 30 and 60 degrees versus wavenumber. This shows the spectral dependence of the reflectivity as well as the dependence on incident angle.

These relationships are based on the electromagnetic theory of light derived from Maxwell's equations. Measurable parameters related to unique refractive indices for materials of interest have been derived through the use of Fresnel's equations.

Polarization

Natural light from the sun is unpolarized. This nomenclature refers to the random orientation of the electric field as it oscillates, meaning there is no preferred direction for the electric field to oscillate. However, when natural light is reflected off a surface or scattered from particles in the atmosphere, the redirected light can become partially or completely polarized as shown in the previous section. A mathematical treatment of polarization decomposes the electric field into x and y components that oscillate transversely to the direction of travel. The key to determining the polarization of a traveling wave is the phase difference term, ε, in equation (3-1). When there is a multiple of π phase difference between the x and y components of the electric field, the light is said to be linearly polarized. If a $\pi/2$ phase difference is present, the light is said to be circularly polarized because the 'lag' that exists between the two components generates a circular pattern as the light propagates. Any other phase difference produces an elliptically polarized beam.

Stokes Parameters and Vectors

To deal with the polarizing nature of reflection and refraction quantitatively, a mathematical description of the polarization of light can be given by four Stokes parameters and a Stokes vector comprised of the parameters. The four states of polarization: unpolarized, linear, circular, and elliptical, can be described using vector notation. With four elements, the Stokes parameters capture all the different polarization states with which an electromagnetic wave can propagate. These four elements can be described in various ways. By measuring transmitted irradiance through a polarizing

element, the following irradiances can be measured, $I_0, I_{90}, I_{45}, I_{135}, I_l,$ and I_r where the subscript refers to the orientation of the polarizing element. I_0 and I_{90} correspond to vertical and horizontal polarization, I_{45} and I_{135} correspond to components oriented at ±45 degrees, and I_l and I_r correspond to left and right circular polarizations. The Stokes parameters can be related to the following way in a Cartesian basis,

$$S_o = \langle E_{0x}{}^2 \rangle + \langle E_{0y}{}^2 \rangle \tag{3-48}$$

$$S_1 = \langle E_{0x}{}^2 \rangle - \langle E_{0y}{}^2 \rangle \tag{3-49}$$

$$S_2 = \langle 2E_x E_y \cos \epsilon \rangle \tag{3-50}$$

$$S_3 = \langle 2E_x E_y \sin \epsilon \rangle, \tag{3-51}$$

where ϵ is the phase difference between components, the $\langle\,\rangle$ brackets indicate a time average, S_o is the incident irradiance of the wave. S_1 indicates the amount of horizontal or vertical linear polarization, S_2 indicates the amount of linear polarization oriented at $+45^o$ and -45° to the vertical axis, and S_3 indicates the difference in right-handedness and left-handedness of elliptical or circular polarizations [1]. The following inequality expresses the relationship between all the parameters

$$S_0^2 \geq S_1^2 + S_2^2 + S_3^2. \tag{3-52}$$

Two important expressions for remote sensing follow from this expression. First is the degree of polarization which is expressed by

$$DOP = \frac{\sqrt{S_1^2 + S_2^2 + S_3^2}}{S_0} \tag{3-53}$$

and the degree of linear polarization (DOLP) which is expressed by

$$DOLP = \frac{\sqrt{S_1^2 + S_2^2}}{S_0} \qquad (3\text{-}54)$$

Simplifying the four Stokes parameters into a 4 X 1 column vector yields Stokes vector.

$$S = \begin{bmatrix} S_o \\ S_1 \\ S_2 \\ S_3 \end{bmatrix} = \begin{bmatrix} \langle E_{0x}{}^2 \rangle + \langle E_{0y}{}^2 \rangle \\ \langle E_{0x}{}^2 \rangle - \langle E_{0y}{}^2 \rangle \\ \langle 2E_x E_y \cos \epsilon \rangle \\ \langle 2E_x E_y \sin \epsilon \rangle \end{bmatrix} \qquad (3\text{-}55)$$

This vector can be normalized by dividing by the total intensity S_o. By doing this, table 2 describes the polarization states for a number of states.

Table 2. Stokes Vectors representing ideal polarization states.

Polarization State	Stokes Vector
Horizontal	$\begin{bmatrix} 1 \\ 1 \\ 0 \\ 0 \end{bmatrix}$
Vertical	$\begin{bmatrix} 1 \\ -1 \\ 0 \\ 0 \end{bmatrix}$
Linear +45	$\begin{bmatrix} 1 \\ 0 \\ 1 \\ 0 \end{bmatrix}$
Linear -45	$\begin{bmatrix} 1 \\ 0 \\ -1 \\ 0 \end{bmatrix}$
Left circular	$\begin{bmatrix} 1 \\ 0 \\ 0 \\ -1 \end{bmatrix}$

Right circular		$\begin{bmatrix} 1 \\ 0 \\ 0 \\ 1 \end{bmatrix}$
Random		$\begin{bmatrix} 1 \\ 0 \\ 0 \\ 0 \end{bmatrix}$

Using Stokes parameters and vectors as a mathematical description of remote sensing measurement is incorporated into the measurements made in this research effort. This approach has broad application across numerous fields of study.

Mueller matrices

In order to provide a quantitative analysis of spectropolarimetric measurements, a mathematical formalism is required. This formalism can be accomplished with two methods, Jones and Mueller calculus. These are two mathematical methods for describing the polarization state of light and how that polarization can change as it interacts with matter [7, 8, 10, 14, 17, 24, 34]. The Mueller matrix approach will be detailed in this section.

The Stokes vector can be normalized by dividing by the total irradiance S_0,

$$ S = \begin{bmatrix} S_o \\ S_1 \\ S_2 \\ S_3 \end{bmatrix} = S_o \begin{bmatrix} 1 \\ s_1 \\ s_2 \\ s_3 \end{bmatrix}, \qquad (3\text{-}56) $$

where S_o, the first element of the Stokes vector, is the only quantity that can be measured directly with an experiment. The transformation of the polarization state of an EM wave

incident on a polarization element is described by the Mueller matrix M, which is a four-by-four matrix of real values

$$M = \begin{bmatrix} m_{11} & m_{12} & m_{13} & m_{14} \\ m_{21} & m_{22} & m_{23} & m_{24} \\ m_{31} & m_{32} & m_{33} & m_{34} \\ m_{14} & m_{42} & m_{43} & m_{44} \end{bmatrix}. \tag{3-57}$$

The effect of an element on an incident polarization state is found by multiplying the Mueller matrix of the element or system M by the incident Stokes vector.

$$S_{out} = M_{sys}S_{inc}. \tag{3-58}$$

The output units are in intensity, the Mueller matrix elements themselves are dimensionless quantities between -1 and 1.

For many optical elements in a system, the effect can be found by multiplying the Mueller matrices of the individual elements in the order that the light encounters them.

$$M_{total} = \prod_{i=1}^{n} M_n = M_n M_{n-1} \dots M_1. \tag{3-59}$$

The Mueller matrix for a polarization element rotated by an angle θ perpendicular to the incident beam is given by the matrix coordinate transformation

$$R(\theta) = \begin{bmatrix} 1 & 0 & 0 & 0 \\ 0 & \cos 2\theta & \sin 2\theta & 0 \\ 0 & -\sin 2\theta & \cos 2\theta & 0 \\ 0 & 0 & 0 & 1 \end{bmatrix} \tag{3-60}$$

This matrix is applied in the order

$$M(\theta) = R(-\theta)MR(\theta), \tag{3-61}$$

where M is the Mueller matrix of the polarizer. Table 3 is several sample Mueller matrices for simple polarizing elements. The ½ in front of these matrices comes from the complete extinction of the orthogonal polarization.

Table 3. Mueller matrices for ideal polarizing elements.

Non polarizing	$\begin{bmatrix} 1 & 0 & 0 & 0 \\ 0 & 1 & 0 & 0 \\ 0 & 0 & 1 & 0 \\ 0 & 0 & 0 & 1 \end{bmatrix}$
Completely depolarizing	$\dfrac{1}{2}\begin{bmatrix} 1 & 0 & 0 & 0 \\ 0 & 0 & 0 & 0 \\ 0 & 0 & 0 & 0 \\ 0 & 0 & 0 & 0 \end{bmatrix}$
Vertically and Horizontally	$\dfrac{1}{2}\begin{bmatrix} 1 & \pm1 & 0 & 0 \\ \pm1 & 1 & 0 & 0 \\ 0 & 0 & 0 & 0 \\ 0 & 0 & 0 & 0 \end{bmatrix}$
Linear ±45	$\dfrac{1}{2}\begin{bmatrix} 1 & 0 & \pm1 & 0 \\ 0 & 0 & 0 & 0 \\ \pm1 & 0 & 1 & 0 \\ 0 & 0 & 0 & 0 \end{bmatrix}$
Left and Right circular	$\begin{bmatrix} 1 & 0 & 0 & \pm1 \\ 0 & 0 & 0 & 0 \\ 0 & 0 & 0 & 0 \\ \pm1 & 0 & 0 & 1 \end{bmatrix}$

Optical devices have inherent polarization preferences which result in measurement errors. These inaccuracies can be accounted for by measuring and calculating the Mueller matrix elements for an optical device and applying them using Mueller calculus to polarization sensitive measurements.

Optical Surfaces

The previous discussion of Fresnel reflectance is based upon ideally smooth surfaces. Including models for surface parameters that affect reflected and emitted light greatly changes the phenomena observed by remote sensing techniques. There are two major types of reflection, specular and diffuse. Specular reflection occurs when all incident light is reflected according the law of reflection, and diffuse reflection evenly distributes incident light into all angles.

Bidirectional Reflectance Distribution Function (BRDF)

Application of the BRDF and polarimetric BRDF (pBRDF) goes beyond the scope of the research presented in this thesis, but a brief overview is included for completeness. In the examples given earlier detailing Fresnel reflectance, the magnitude of the reflectance was determined solely by the material property, namely the complex index of refraction and the angle of incidence. These examples only apply to ideal smooth surfaces. To achieve a more realistic example, surface imperfections must be included in modeling. This is accomplished in a statistical manner by assigning a Gaussian distribution to the parameters associated with micro surfaces. Allowing for Fresnel's equations to still be applied on a smaller scale, and averaged over the distribution gives a more accurate picture of real reflections. To illustrate the differences in the types of reflections, figure 8 shows how incident light gets reflected for three different surface types.
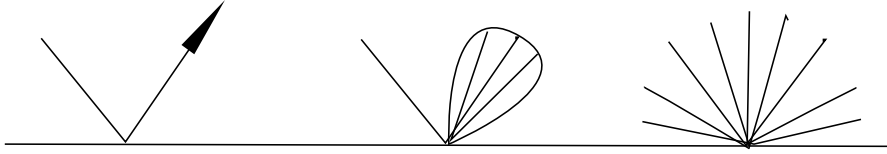
Figure 8. From left to right: Specular reflection, nearly specular, and completely diffuse reflection.

A good example of specular reflection is a metal mirror and an example of a diffuse reflector would be a painted wall. The BRDF quantifies the radiance scatter into all direction from a source above the material of interest. The equation for the BRDF is in units of $[sr^{-1}]$ and is given by

$$f_r(\theta_i, \phi_i, \theta_r, \phi_r, \lambda) = \frac{dL_r(\theta_r, \phi_r)}{dE(\theta_i, \phi_i)} \qquad (3\text{-}62)$$

where L_r is the surface leaving spectral radiance $\left[\frac{W}{m^2 * sr * \mu m}\right]$ and E is the spectral irrandiance $\left[\frac{W}{m^2 * \mu m}\right]$. The geometery associated with these measurements is displayed in Figure 9 below.
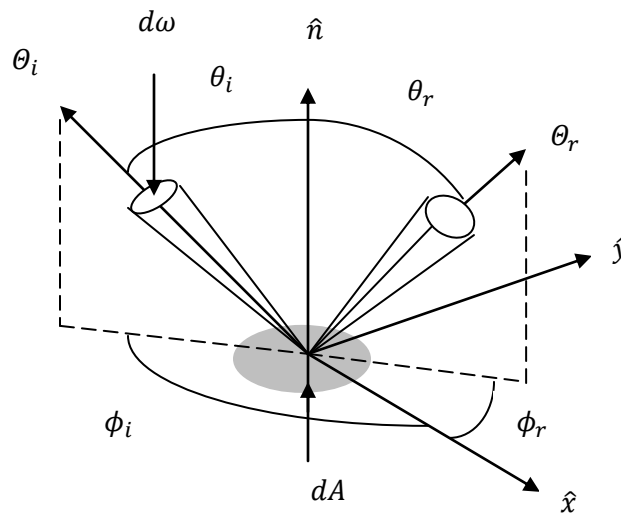
Figure 9. The BRDF geometry is characterized by four angles corresponding to the incident and reflected light in planes perpendicular and parallel to the surface.

If emission in the LWIR is desired over reflectance at shorter wavelengths, then Krichoff's law can be used which relates emission and reflection by the following equation for surface in thermal equilibrium

$$\varepsilon = 1 - r. \tag{3-63}$$

Using this relationship, the BRDF models developed for reflectance can be adapted for the thermal infrared. Additional effects such as shadowing and obscuration due to the heights of the surface roughness features can be incorporated to improve accuracy but are second order effects. The BRDF model simply quantifies the ratio of incident EM radiation to the reflected portion.

Polarization can be incorporated into the BRDF model. The polarization BRDF (pBRDF) includes a polarized specular component and an unpolarized volume component [25]. The polarized component of the BRDF is comprised of a 4 x 4 Mueller matrix while the unpolarized component is a scalar value [15]. In order to account for the specular component, a statistical distribution of a Fresnel reflection Mueller matrix is used to describe the micro surfaces associated with a material. Figure 10 shows how incoming parallel rays get reflected in a distribution of direction due to the different slopes of the microfacets.

Diffuse Reflection
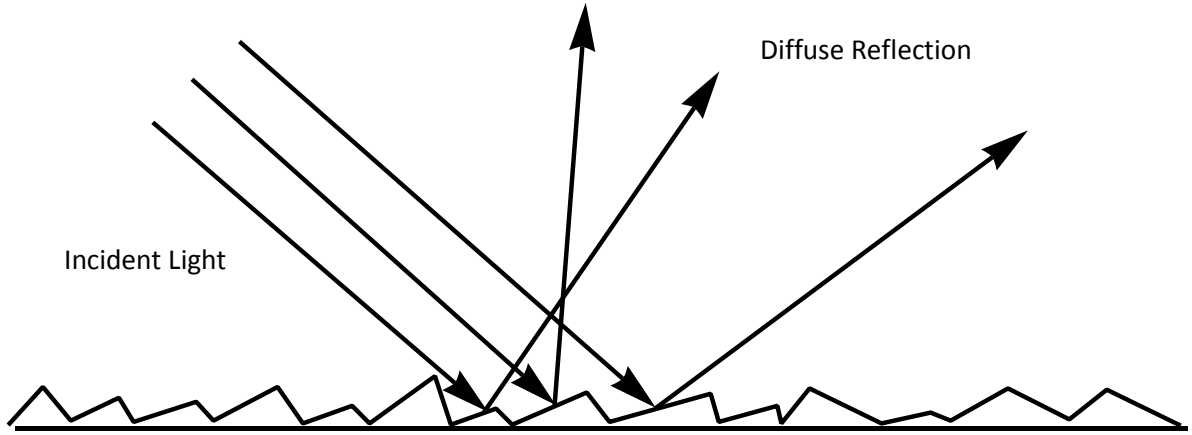
Incident Light

Figure 10. Graphic showing how parallel incoming rays of light interact with a rough surface. Each micro facet is governed by Snell's law. Depending of the angle of incidence and slope of the micro facet, the reflected light will be diffuse.

A common Gaussian distribution is often used to statistically describe the spread in surface slopes and roughness. This distribution of surfaces has an impact on the DOLP observed. For a Gaussian distribution, the ratio of a rough surface to a smooth surface's DOLP is given by

$$\frac{P(rough)}{P(smooth)} = \frac{5}{m_0^2} - \left(\frac{5}{m_0^2} + \frac{3}{2}\right)\frac{\sqrt{\pi}}{2}e^{\frac{1}{m_0^2}} \cdot erfc\left(\frac{1}{m_0}\right) \quad [2].$$

(3-65)

This ratio lowers the theoretical DOLP of a smooth surface based on the value of the surface parameter. For a given surface roughness parameter m_0, which is the root mean squared (RMS) of the micro facet slopes, figure 11 shows how the DOLP is altered.

41
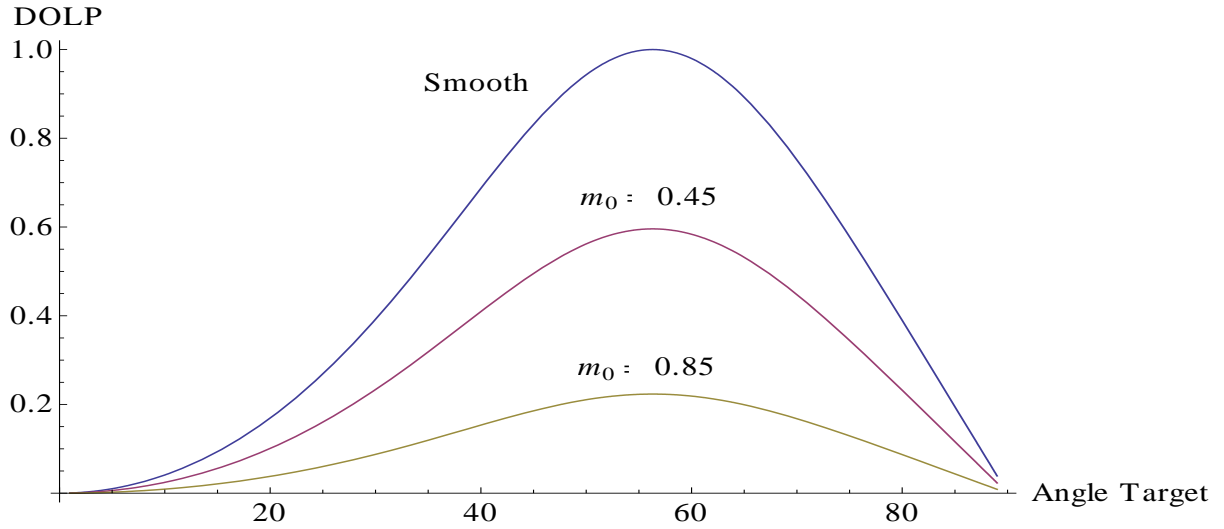
Figure 11. DOLP for glass for three different RMS values for surface roughness showing the decreasing DOLP for rough surfaces for all incident angles.

Multiple layers

At every change in index of refraction, some light will undergo a reflection. For a thin absorbing material on the surface on a reflecting material, the air-to-thin-layer interface will cause reflections between the bottom material and the air-to-thin-layer interface as shown in figure 12. The summation of the EM radiation that is reflected off the top thin layer and reflected multiple times off the bottom layer can be summed in apparent reflection. R_{12} is the reflection from the top layer, the refractive index of air is assumed to be one. R_{21} is equal to R_{12}, and R_{23} is the reflection from the change in index from the thin layer and bottom layer. This apparent reflectance is given by

$$\rho(\lambda) = \frac{R_{12}{}^2 + R_{23}{}^2 + 2R_{12}R_{23}\cos 2\beta}{1 - R_{21}{}^2 R_{23}{}^2 + 2R_{12}R_{23}\cos 2\beta}, \text{[15]} \qquad (4\text{-}9)$$

where β is the absorption coefficient for the material defined as

$$\beta = \frac{2\pi n_2 \, h\cos\theta_2}{\lambda}. \qquad\qquad (4\text{-}10)$$

The above equations are for absorbing materials, and can be extended to include polarization by incorporating the Fresnel reflections for each surface.

Extending this model to include polarization Fresnel's equations can be applied to both layers. An example will be given for an Aluminum surface with a thin layer of Aluminum Oxide on top due to the relevance to the research conducted. DOLP is a function of incident angle, and the refraction from the oxide layer changes the incident angle for the aluminum surface. The reflected perpendicular and parallel electric field vectors can be generated using the same methods that derived equation (4-9).
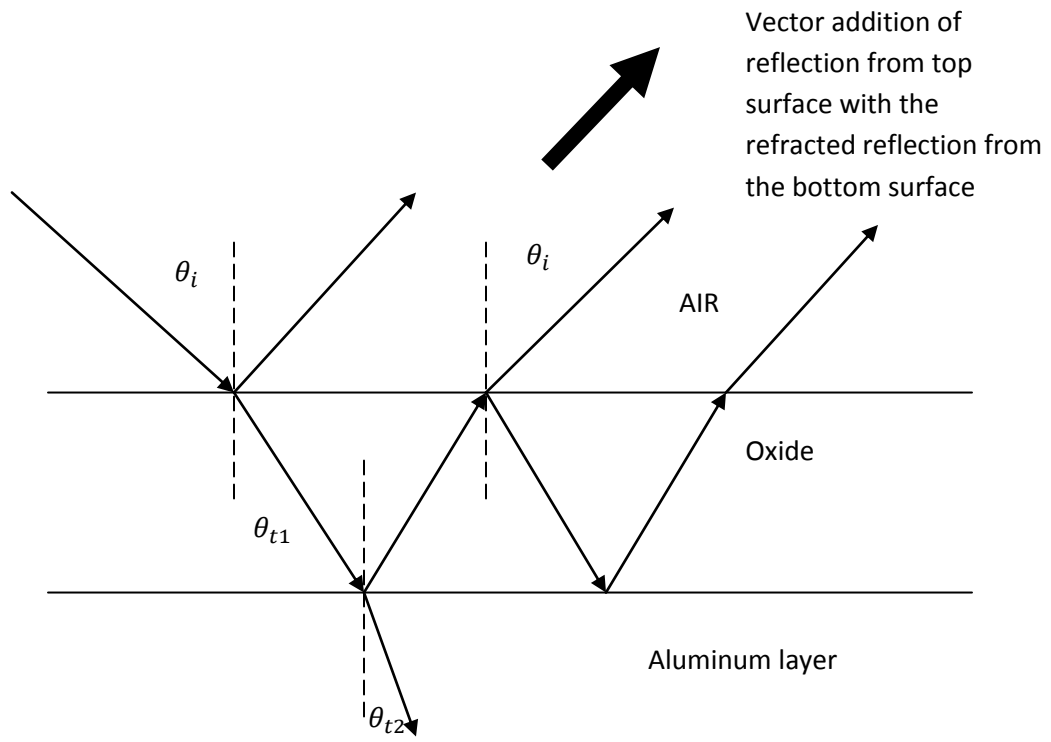
Figure 12. Combination of reflections for thin layer of oxide on top of aluminum surface.

Pure aluminum oxidizes in the atmosphere causing a thin layer of aluminum oxide to build up on the surface. Typically, this is very thin, approximately tens of nanometers thick [38]. Aluminum oxide is a dielectric, making the imaginary component of the refractive index nearly zero. As a result, the thin top layer does not absorb any of the EM radiation. Figure 13 is real part of the index of refraction and reflective properties for aluminum oxide $[Al_2O_3]$
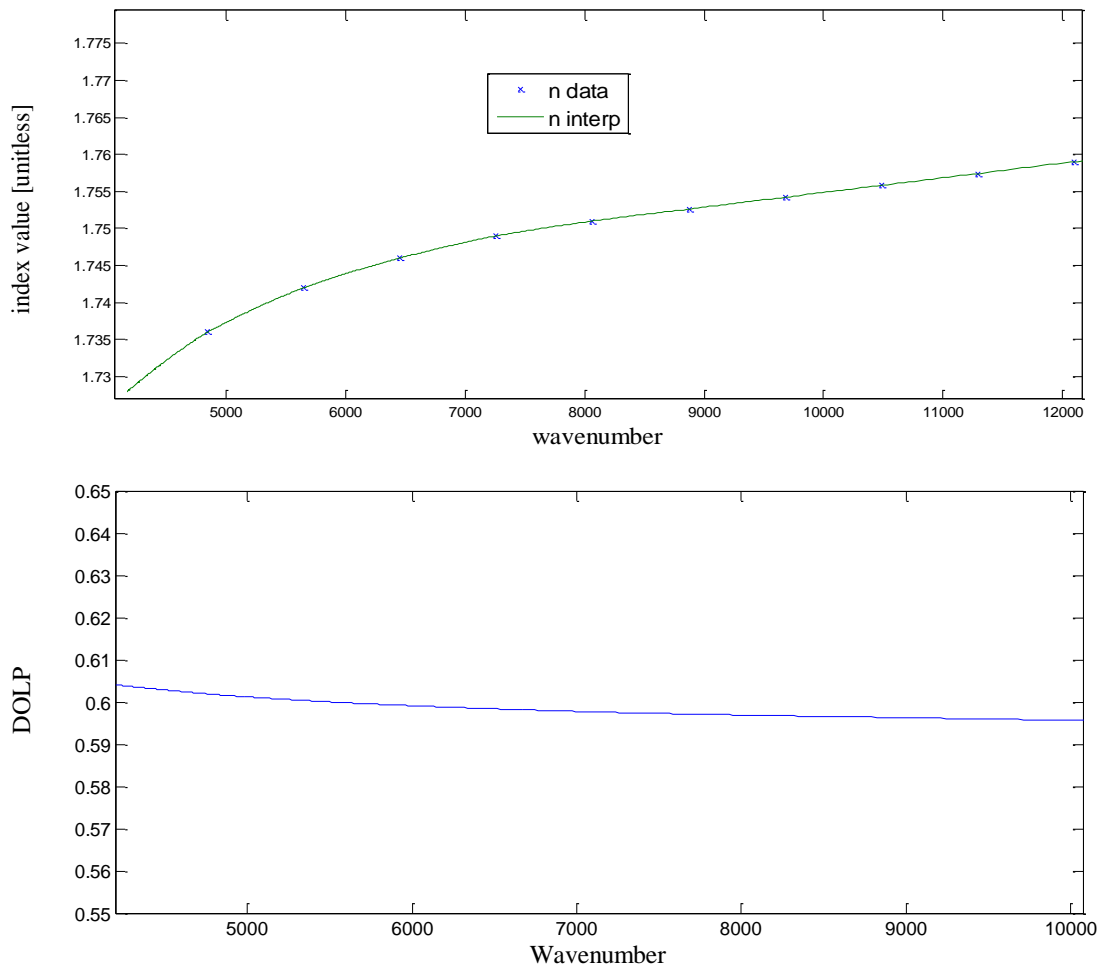
Figure 13. DOLP for Aluminum Oxide at incident angle of 40 degrees. While this DOLP is high compared to pure Aluminum, only a small fraction contributes to the total DOLP.
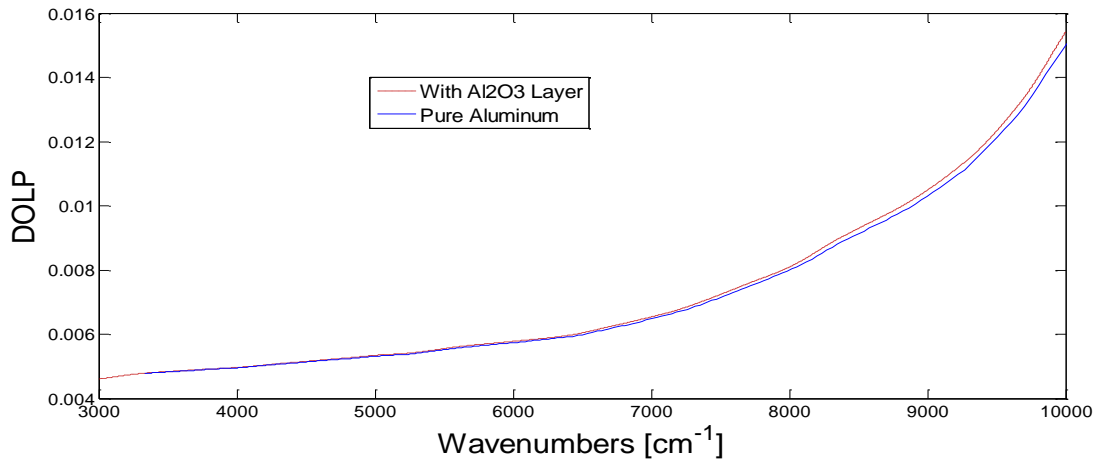
Figure 14. DOLP of Aluminum with a layer of Aluminum Oxide on top at an incident angle of 40 degrees. The layer of Aluminum Oxide is 50 nm.

Aluminum Oxide by itself can produce a high reflected DOLP compared to Aluminum. However, since it is a non absorbing material, most of the light is transmitted through the thin layer. As a result, the reflective components from the thin layer are small compared to the reflective components from the Aluminum layer which leads to a small increase in the DOLP reflected which can be seen above in figure 14. This show the Aluminum layer's DOLP to be the dominate factor in the two layer model with a thin dielectric surface.

Fourier Transform Infrared Spectrometers (FTIR)

There are several methods for obtaining spectral information. Most use a dispersive element or grading to separate the wavelengths of light. However, the Fourier transform spectrometer is based on the Michelson interferometer which has several advantages [16]. For example, incoming light is split in two directions by a beam splitter, reflected and recombined on a detector. The path length of the moving mirror determines the spectral resolution, which is much shorter than the equivalent size of a prism. This

45

gives FTIRs an inherent broadband capability. Based upon the material used in the detector array, the spectral range can cover from the visible to LWIR.

Core to the operation of a FTIR is a Michelson based interferometer. As light enters the instrument, one mirror is fixed while the other scans creating an optical path length difference (OPLD) between the two mirrors as shown in figure 15.
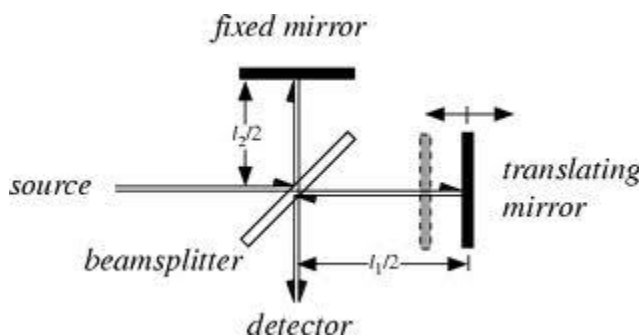
Figure 15. Michelson Interferometer

All wavelengths entering the interferometer will then either constructively or destructively interfere based upon wavelength and OPLD. This creates what is called an interferogram at detector. Spectral information is retrieved by taking the Fourier transform of the interferogram.

In order to know precisely where the moving mirror is at all times, a Helium-Neon laser which operating at 15798 cm^{-1}, is used in the Bomem FTIR. This monochromatic light source generates a sinusoidal interferogram that is detected and converted into a digitized form to monitor the OPLD. This fringe pattern is used to trigger an analog-to-digital conversion to sample the signal. When the fringe crosses zero, in either positive or negative direction, the sampling is triggered. If the interferogram is sampled more frequently than the HeNe wavelength, that is called

oversampling. This is useful when light collected by the detector is outside of the spectral range of interest. If the full wavelength of the He-Ne laser is used to sample the data, only half of the full spectral range of the FTIR will be used. To sample the full spectral range, oversampling needs to be turned on, and half of the He-Ne wavelength needs to be used to process the spectral data. If not, the spectral information collected at wavenumbers below half the He-Ne wavelength will be mirrored. Figure 16 shows the correct spectrum with oversampling on.
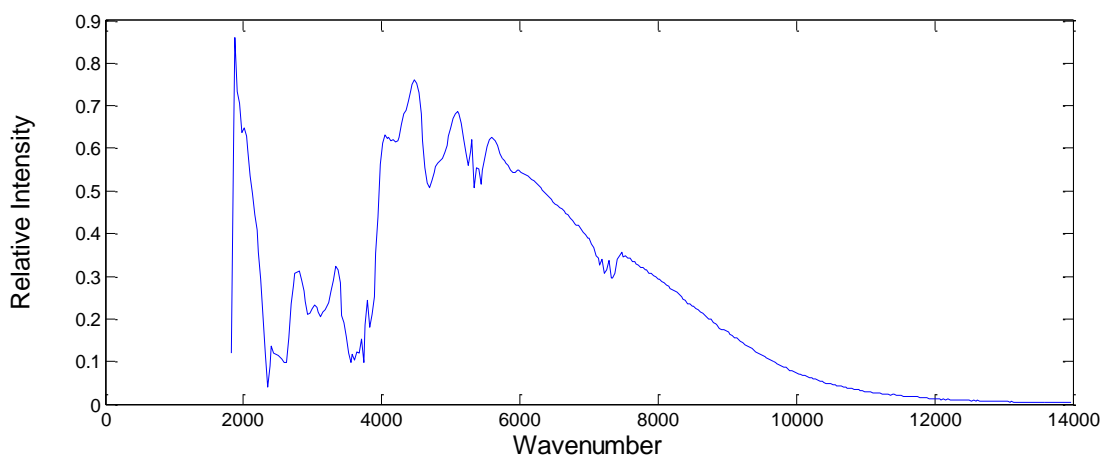
Figure 16. Raw measurement of a Spectralon integrating sphere with oversampling on using half the He-Ne wavelength removing the symmetry in the NIR.

At zero path length difference (ZPD), all wavelengths of light entering the FTIR constructively interfere which corresponds to a spike in the middle of the interfereogram. In order to establish a zero path difference, the instrument contains a white-light source to generate the spike in the interfereogram which sets the ZPD.

The inherent advantages designed into FTIR spectrometers make them ideal for collecting polarimetric signals, because of their broadband capability. In order to

accurately measure the spectra phenomena, calibration must be performed. Calibration of a radiometer is based on a linear instrument response as shown in figure 17.
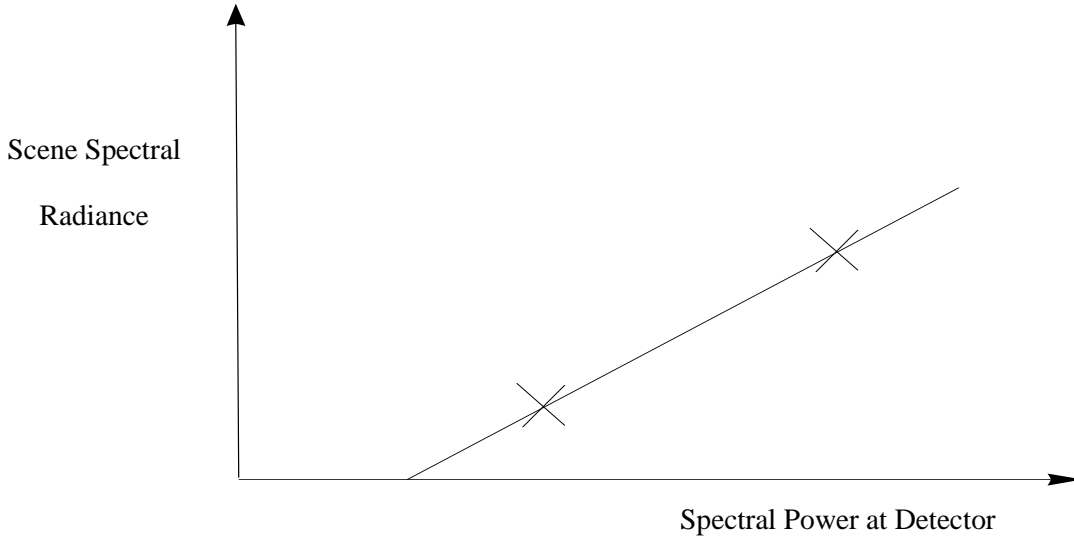
Figure 17: Linear relationship between the scene spectral radiance and the power at the detector. Where the power crosses the x-axis is below the instruments spectral response.

The instrument is assumed linear, i.e. the signal out of the detector is proportional to the power reaching it. Two distinct calibration sources are necessary so that radiant power arising from within the instrument can be distinguished from that of the source while also determining the response function. The measured radiance can be described by the following expression

$$S_{measured}(\sigma) = G(\sigma)\big[L_{source}(\sigma) + L_{offset}(\sigma)\big], \qquad \text{3-66}$$

where σ is the wavenumber, $S_{measured}$ is the measured spectrum, $G(\sigma)$ is the response function of the instrument or gain, L_{source} is the scene radiance, and L_{offset} is due to any background or offset. In order to determine $L_{source}(\sigma)$, solving a system with two unknowns requires making two measurements of a known source. By measuring the

radiance from a blackbody at two different temperatures this can be accomplished. The solutions for the gain and offset terms are as follows

$$G(\sigma) = \frac{S_{Hot} - S_{cold}}{L_{Hot} - L_{cold}} \qquad \text{3-67}$$

$$L_{offset} = \frac{L_{Hot} \cdot S_{cold} - L_{Cold} \cdot S_{Hot}}{S_{Hot} - S_{cold}}. \qquad \text{3-68}$$

After making these measurements, the gain and offset can be applied to measured spectrum by

$$L_{source}(\sigma) = \frac{S_{measured}(\sigma)}{G(\sigma)} - L_{offset}. \qquad \text{3-69}$$

In practice, thermal instrument drift, non ideal sources, and other sources of error limit the accuracy of this calibration method. In order to make accurate spectropolarimetric measurements, these calibration efforts are important.

Summary

For all remote sensing applications, it is important to know fundamentally how photons are generated from a source, interact with matter, transfer through the atmosphere to an instrument, and how the instrument manipulates the final signal. By understanding the wave nature of light, and how that light behaves upon reflection or emission, valuable information can be obtained from targets of interest. Using mathematical techniques pioneered by Stokes and Mueller, processing measureable quantities is possible. Finally, understanding the limitations and operation of how

spectrometers alter and process EM signals is critical to understanding the information

collected.

IV. Spectropolarimetric methodology and FTIR measurements of aluminum and glass

Introduction

This chapter details the method employed to infer the DOLP from three samples and the results of those measurements. The procedure for relative polarimetric calibration is detailed along with the limitations of this method. Limitations of the equipment used are also addressed. The experimental set up is described in detail along with the procedure for ensuring accurate alignment.

Relative Intensity Polarimetric Calibration

Each reflection from and transmission through an optical element contributes to a polarization preference in the FTIR. This effect in the FTIR is substantial and must be accounted for. Figure 16 shows the polarization preference of the Bomem FTIR spectrometer with a Thorlabs ZeSn wire gird polarizer. The spectral range of this polarizer is 2-20 μm or 500-5000 wavenumber (cm^{-1}) and extinction ratio of 105 at 3 μm and increases with wavelength. These measurements were taken using a wide area blackbody and the raw, uncalibrated was data averaged over the spectral range of interest for this experiment (4000-1000 cm^{-1}). Each orientation of the polarizer was divided by the intensity measured with the polarizer at zero degrees because that is the minimum.
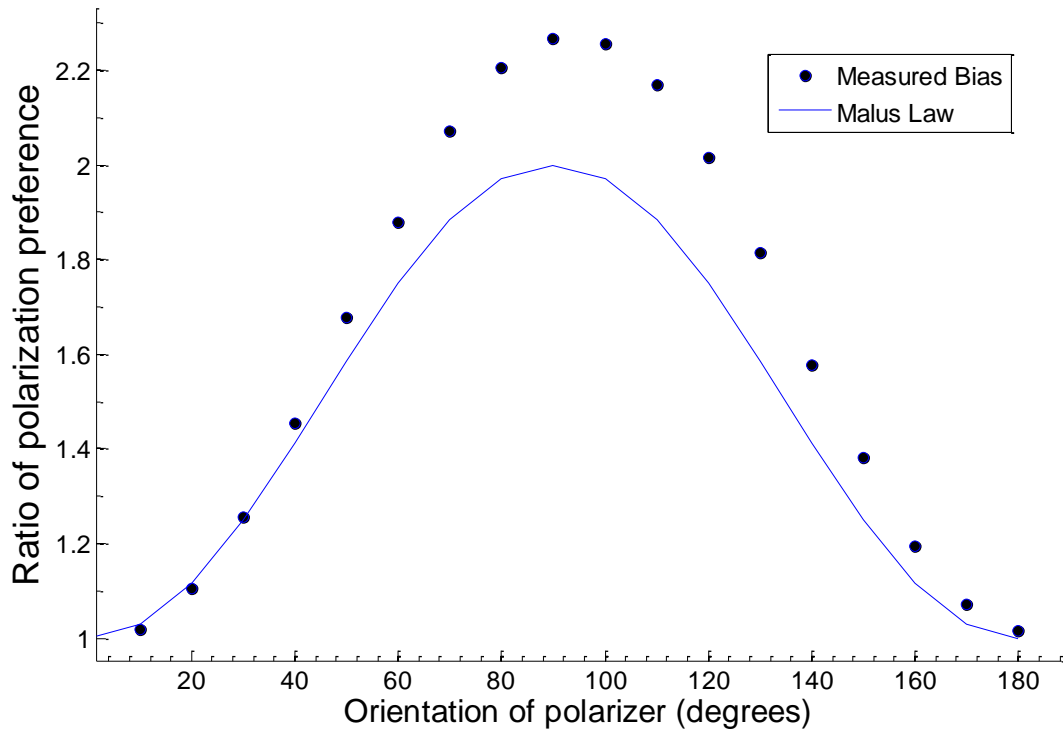
Figure 18. Measurements of a wide area blackbody through a wire grid polarizer rotated by 10 degree increments with a Bomem 254 FTIR spectrometer. The polarization response is plotted as a function of angle showing a maximum 90 degrees which indicates that the FTIR has a high transmission for electric field oriented in that direction. Deviations from Malus' Law, shown with a phase shift, indicate a higher transmission of light at the corresponding polarization orientation.

Malus' Law, shown below in figure 19, predicts the intensity through a fixed polarizer (effectively the optics within the FTIR) and a rotating polarizer and is proportional to cosine squared. Measuring this effect over a 360 degree period repeats the pattern over 180 degrees indicating that there is no difference between measurements taken 180 degrees apart. There is a slight asymmetry in the measured data which indicates a drift in calibration of the time period of the measurements taken. This matter is addressed later in this section.
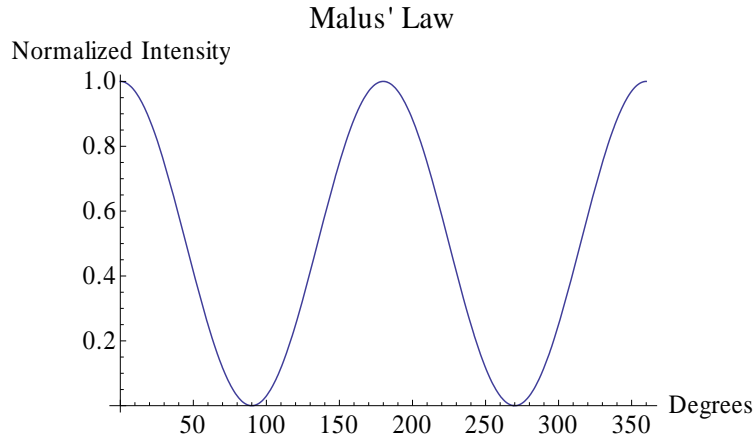
Figure 19. Malus' law showing the change in intensity through two polarizers as one
is rotated. This affect is analogous to using a wire-grid polarizer and a FTIR
spectrometer where the FTIR is a fixed polarizing element.

Rotating a wire-grid polarizer while looking at an unpolarized source, such as a wide-area

blackbody or an integrating sphere, provides the information necessary to compensate for

the polarization preference inherent in the FTIR. This measurement also incorporates the

transmission and extinction ratio of the polarizer. This is accomplished with the simple

set up shown in figure 20.
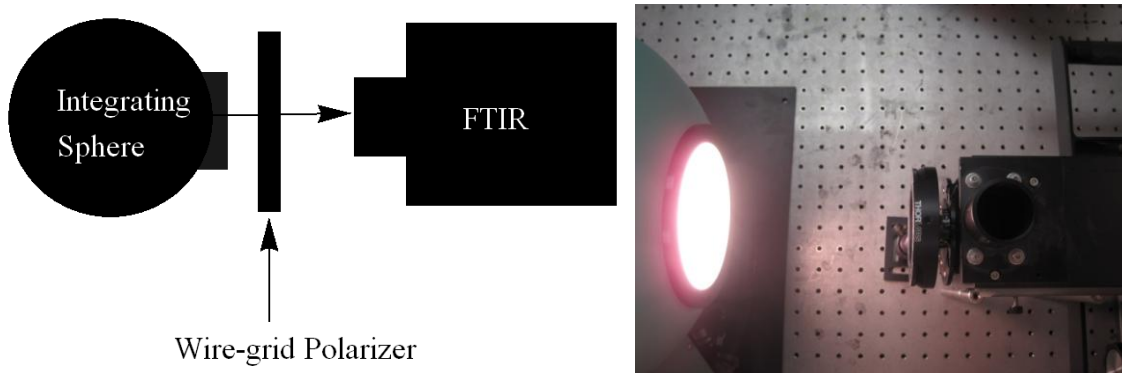
Figure 20. Polarimetric Calibration Set Up

Treating the polarizer and FTIR as one instrument, each polarizer orientation is effectively a different instrument due to the combination of polarized light passed by the polarizer and the inherent preference of the FTIR. Therefore, each of these polarizer orientations has different transmission associated with them which are a function of wavelength. This procedure can be extended to include circular polarization by adding a quarter wave-plate between light source and wire grid polarizer [8]. Circular polarization can be ignored in this experiment because the emitted circular polarization from the integrating sphere is negligible. There should be no linear polarization preference for black bodies or integrating spheres either. To test this assumption, a FLIR imaging camera was used to measure the relative intensities measured for four different orientations of the wire grid polarizer. Table 4 shows these results.

Table 4. Polarimetric biases of the FLIR imager. These measurements indicate a polarized emission of 2-4 percent relative to the intensity measured with the polarizer at zero degrees.

	45 Degrees	90 Degrees	135 Degrees
Relative intensity to degree = 0	1.02	0.97	0.96

Self emission fluctuations from the FTIR can cause significant errors in the calibration. This occurs for two reasons: first, changes in the beam splitter temperature cause an expansion in the material which results in a difference in path length; second, changes in the temperature affect the amount of self emission that results in an offset to the calibration. Even after several hours of operation, the Bomem FTIR does not come to

a stable temperature. The data collected in figure 17 was collected by recording the beam splitter temperature over three hours of operation at regular intervals.
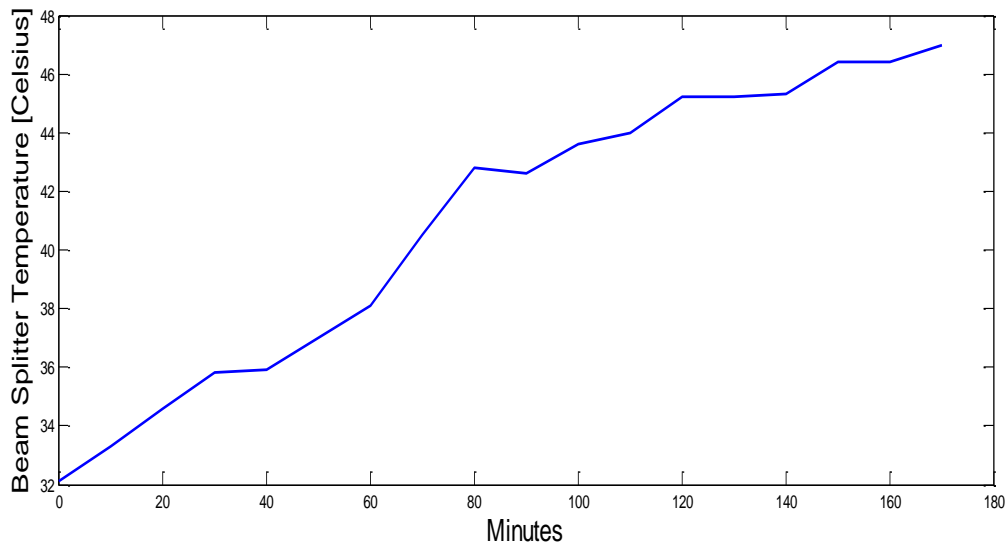
Figure 21. Temperature variation in the beam splitter versus minutes of operation. Showing that the instrument does not come to a steady state.

This effect is mitigated by collecting data outside the spectral range of the Bomem's self emission or by leaving the machine on overnight to reach a more stable operating temperature of 54 degrees Celsius. Spectropolarimetric data is analyzed in the 1 to 2.5 micron range or 4000 to 10000 wavenumbers for this reason. Figure 22 shows the relative intensity of the self emission of the FTIR. The instrument does not have a response below 1800 wavenumbers.
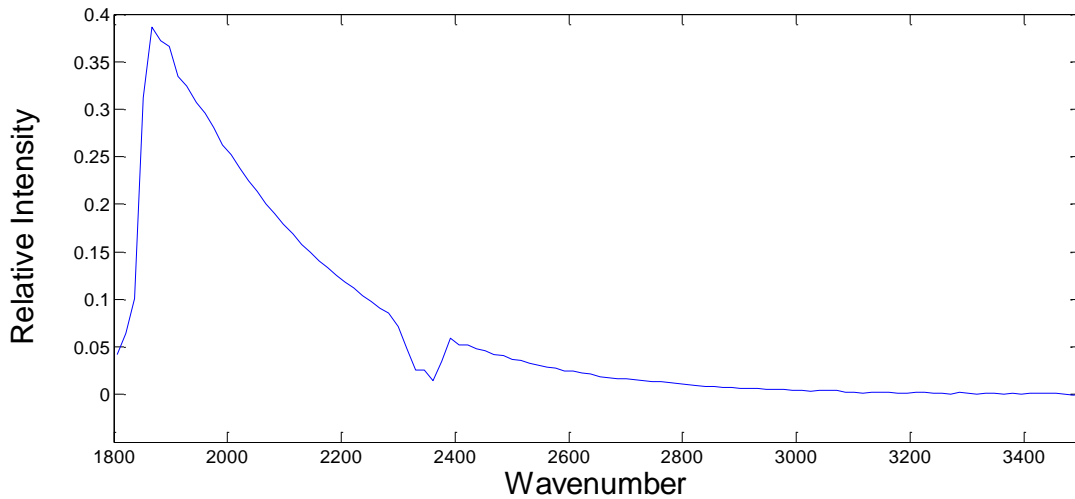
Figure 22. Self emission of Bomem FTIR. This black body like emission changes as a function of the instrument's temperature which changes enough over the time scales of the data collection to be a significant source of error at wavenumbers below 3200 cm^{-1} . The dip at 2300 wavenumber is due to CO2 absorption.

Accounting for the polarization preference, changing self emission of the instrument, and thermal expansion of the beamsplitter must be accounted for to make accurate spectropolarimetric measurements.

Relative Polarimetric Calibration Data Collection

Polarization biases are functions of wavelength because the transmission, reflection, emission, and absorption of the optical elements within the FTIR are also wavelength dependent. To measure the Stokes parameters in this experiment, four measurements are needed. By measuring the intensity of a constant light source through a polarizer at four different orientations, 0, 45, 90, and 135 degrees, the spectro-polarization preferences can be accounted for and applied to remove the polarimetric response of the instrument. This measurement is defined in the following way

$$Y_\theta(\sigma) = B_\theta(\sigma)G(\sigma)(L(\sigma) + O(\sigma)) \qquad (4\text{-}1)$$

where Y is the raw signal, θ denotes the orientation of the polarizer, B is the polarimetric bias, G is the instrument gain, L is the emission of the light source, O is the offset due to self emission of the instrument, and σ represents wavenumber. Making measurements above 4000 wavenumbers eliminates the offset and simplifies the equation to

$$Y_\theta(\sigma) = B_\theta(\sigma)G(\sigma)L(\sigma). \qquad (4\text{-}2)$$

By taking the ratio between two polarizer orientations, the instrument gain and light source cancel, and the polarimetric bias for that orientation is determined. Setting the bias for the polarizer orientation at zero degrees to equal one allows for all other angles to be made relative to that measurement

$$\frac{Y_\theta(\sigma)}{Y_{\theta=0}(\sigma)} = \frac{B_\theta(\sigma)G(\sigma)L(\sigma)}{B_{\theta=0}(\sigma)G(\sigma)L(\sigma)} = \frac{B_\theta(\sigma)}{1}. \qquad (4\text{-}3)$$

Using these measurements, a relative polarimetric calibration can be achieved if the instrument gain, polarimetric bias, and light source are stable.

Since the degree of linear polarization is a measurement of relative intensity, the ratio of these measurements can be applied to scale the same four measurements when measuring a polarized scene. For example, determining the bias for the FTIR and polarizer at 90 degrees, the signal measured at that polarizer position is divided by the signal measured with the polarizer oriented at zero degrees. The same procedure is followed with polarizer positions at 45 and 135 degrees, and the biases (B) are defined in the following way

$$B_{45}(\sigma) = \frac{Y_{45}(\sigma)}{Y_0(\sigma)}; \quad B_{90}(\sigma) = \frac{Y_{90}(\sigma)}{Y_0(\sigma)}; \quad B_{135}(\sigma) = \frac{Y_{135}(\sigma)}{Y_0(\sigma)}, \tag{4-3}$$

where Y is the measurement described in equation (4-2). These ratios are wavelength dependent and therefore allow corrections over the spectral range where instrument self emission is not a problem. Figure 23 shows the spectral dependence of these relative ratios of the polarimetric preference of the Bomem FTIR.
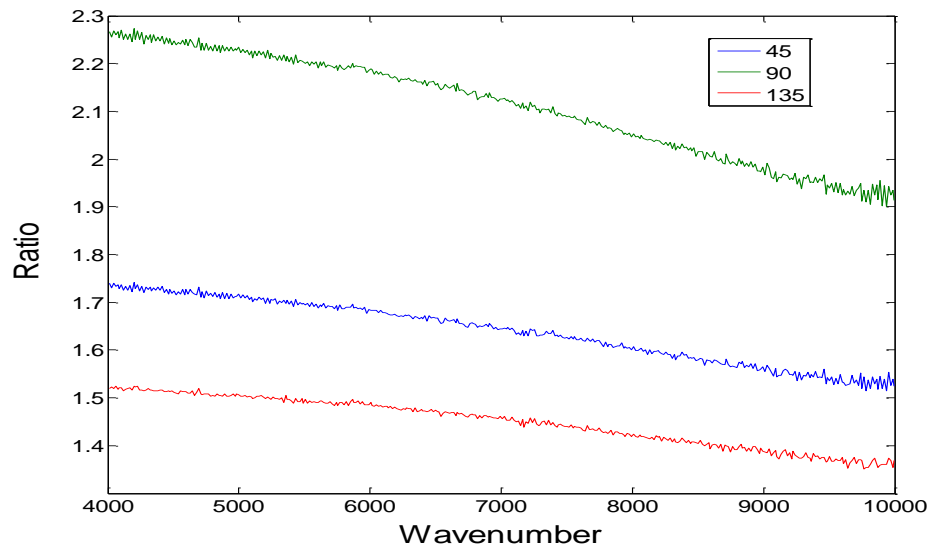
Figure 23. Relative polarimetric bias measurements showing the difference in intensity while measuring a constant source. These spectrally dependent ratios must be applied to spectropolarimetric measurements to remove the polarization preference of the FTIR.

To correct for the polarization bias for the DOLP calculation, the calculated bias is applied to the appropriate measurement to remove polarization bias of the FTIR. DOLP is measured by

$$DOLP = \frac{\sqrt{S_1^2 + S_2^2}}{S_0} \tag{4-4}$$

Where S_0, S_1, and S_2 are the Stokes parameters which are measured in the following way,

$$S_0 = L_{90} + L_0 \tag{4-5}$$

$$S_1 = L_{90} - L_0 \tag{4-6}$$

$$S_2 = L_{135} - L_{45}, \tag{4-7}$$

where L is the polarimetrically calibrated signal measured at the four different polarizer positions. Since DOLP is a relative measurement, absolute radiometric calibration is not needed. With an ideal polarizer, S_0 captures both components of the electric field in the plane of oscillation, while S_1 and S_2 measure the amount of linear polarization by taking the difference of the electric field components. Figure 24 shows the second Stokes parameters for data collect from the Aluminum target at 40 degrees incident. The polarimetrically calibrated signal measured at 45 and 135 degrees are nearly equal making S_2 negligible.
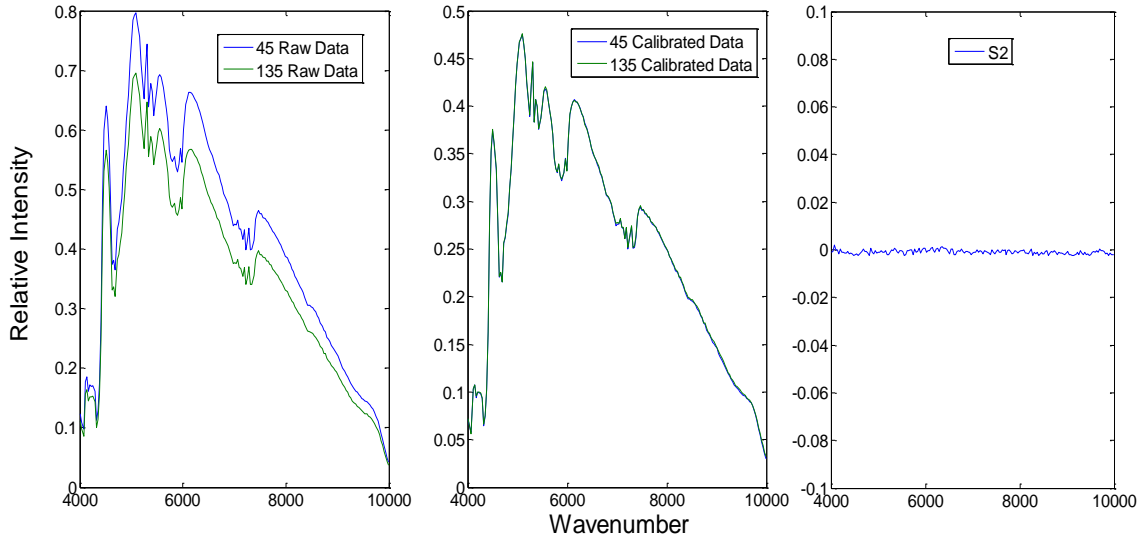
Figure 24. The first plot raw signal measured and the second is the polarimetrically calibrated signal of the integrating sphere reflected off Aluminum with the polarizer oriented at 45 and 135 degrees. These generate the second Stokes parameter and in the third plot which is nearly zero.

With the second Stokes parameter negligible, the DOLP calculation simplifies to

$$DOLP = \left| \frac{L_{90} - L_0}{L_{90} + L_0} \right| \tag{4-8}$$

where L is the raw signal. Using the relative measurements defined in equations (4-3) to remove the polarimetric response of the FTIR, the polarimetrically calibrated DOLP is defined in the following way

$$DOLP = \left| \frac{Y_{90}/B_{90} - Y_0}{Y_{90}/B_{90} + Y_0} \right|. \tag{4-9}$$

Where Y_{90} and Y_0 is the signal measured with the polarizer oriented at 0 and 90 degrees and the biases are defined in equation (4-3). Equation (4-9) represents a polarimetrically calibrated measurement of the FTIR.

The polarimetric response of the FTIR drifts with temperature, affecting the stability of the polarimetric calibration. This can be seen in figure 25 where the ratio of signal measured for polarizer orientation of 0, 45, 90, and 135 degrees change with beam splitter temperature.
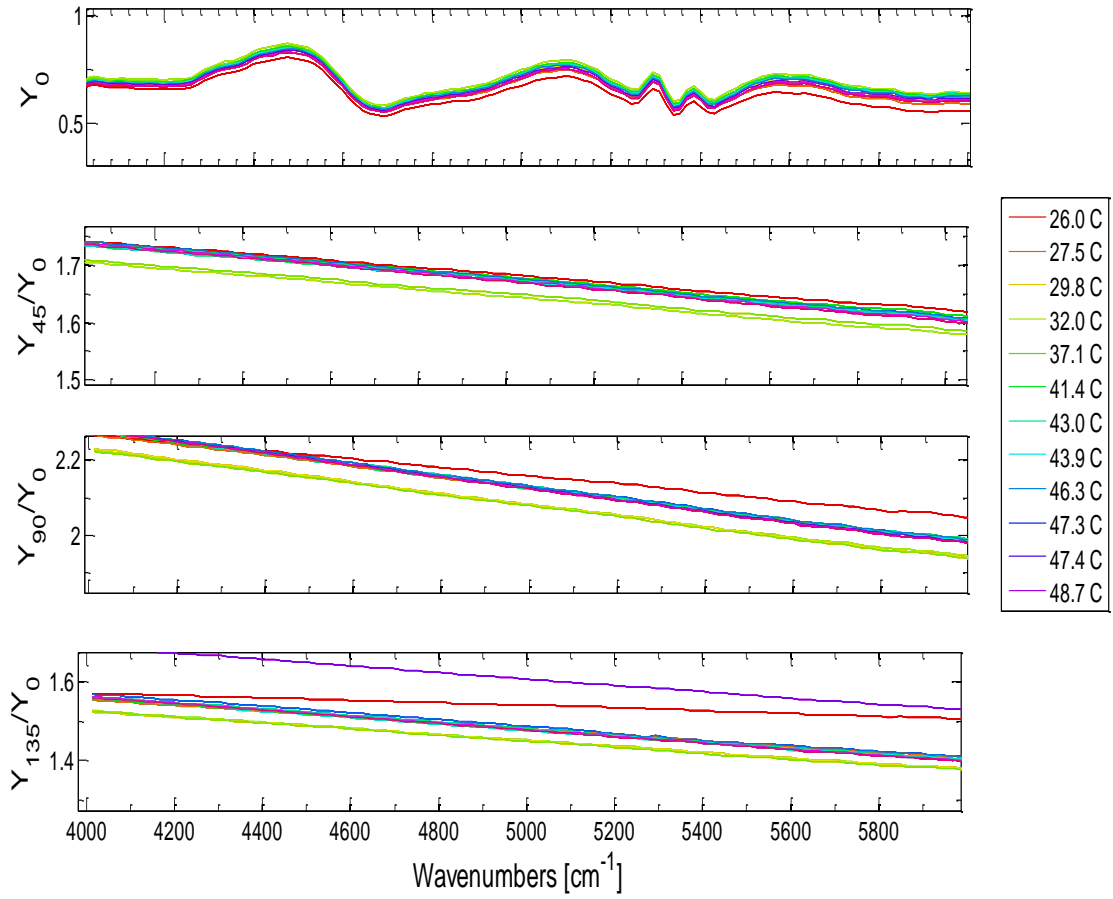
Figure 25. Polarimetric calibration drift for different beam splitter temperatures. Y_0 is the raw measured spectrum with the polarizer set to zero degree. These plots show the ratio of raw measurement taken for different instrument temperatures. This change in calibration shows the instrument temperature dependence of the polarization bias of the FTIR.

Each of the measurements was made at 10 minute increments. This drift in calibration is attributed to the functionality of Michelson based interferometers. Due to the thermal

expansion of the beam splitter, the optical path length is changed along with the optical properties of the material. This sensitivity to temperature will limit the overall accuracy of spectropolarimetric measurements made with FTIR instruments. These factors associated with the polarizer also apply to the glass measurement made.

DOLP data collection

To investigate the spectropolarimetric properties of a material, the following experimental set up is used. An unpolarized source of light from an integrating sphere is incident on the target material. The reflected light becomes partially polarized upon reflection and is passed through a polarizer, and finally into the FTIR. To avoid the fluctuations of the self emission of the instrument, the spectral range of the measurements was reduced to exclude that region. No detectable background radiance was present outside of the self emission region which ensures that any signal that enters the detector is reflected from the sample. This set up is graphically displayed in Figure 26.
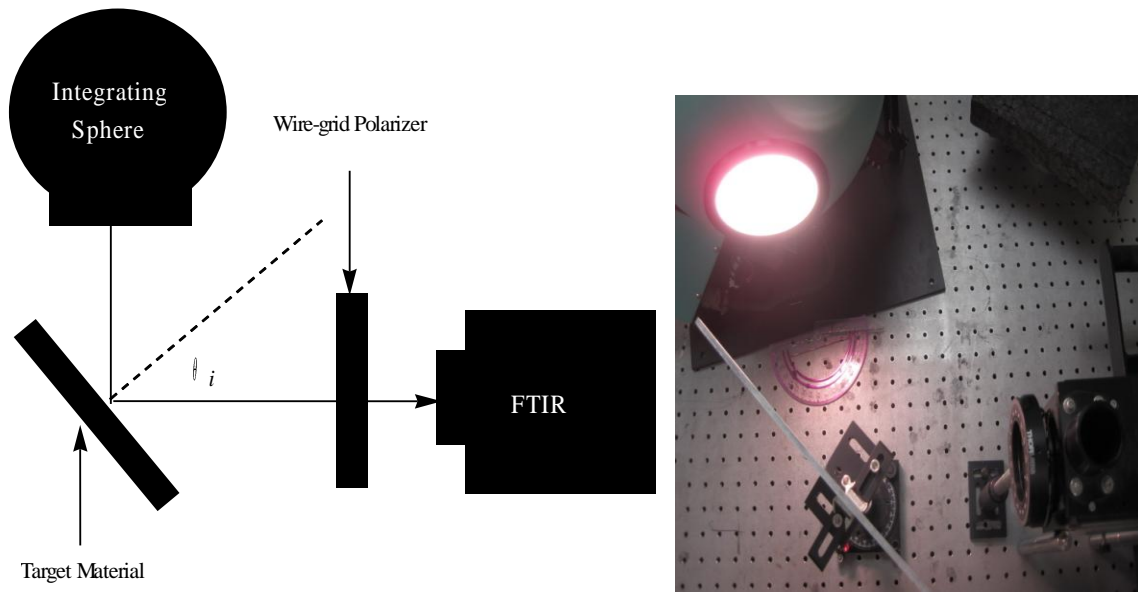
Figure 26. Spectro-Polarimetric Measurement Set Up

Incident angle plays a strong role in the reflection coefficient; therefore careful measurements of the incident angle are required. This was accomplished by inserting the target material in a mount attached to a rotatable plateform with two degree angular measurement marks. To assist in alignment, the holes of the optics table were used to align the center of the target with the entrance aperture of the FTIR. Figure 27 shows how the Aluminum target was aligned to the optics table with two posts. The incident angle is measured from the normal to the surface of the target. Due to its size and weight, the FTIR is kept in place while the incident angle was incremented by 10 degrees. As a result, the integrating sphere needed to be moved by twenty degrees per measurement to maintain the proper incident angle to the target material. These angles were measured using a protractor with one degree markings, and aligned with the holes on the optics

table parallel to the center of the target and entrance of the FTIR which can be seen in figures 28 & 29.

Figure 27. Squaring aluminum plate with optics table grid.

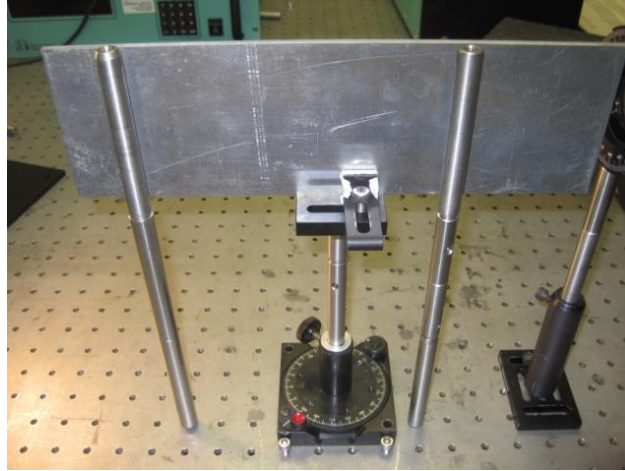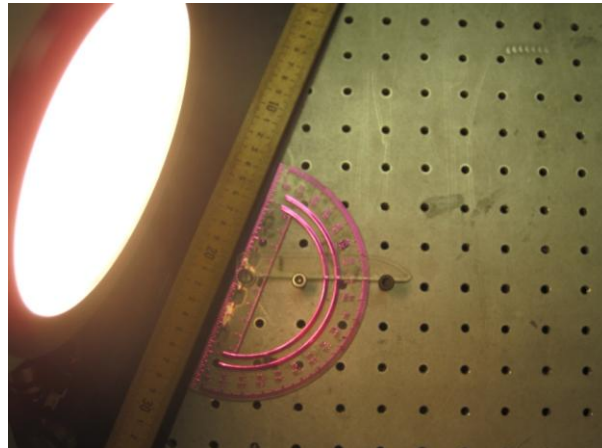**Figure 28. Example of alignment of integrating sphere relative to the optics table grid at an incident angle of 80 degrees relative to the normal of the aluminum surface.**
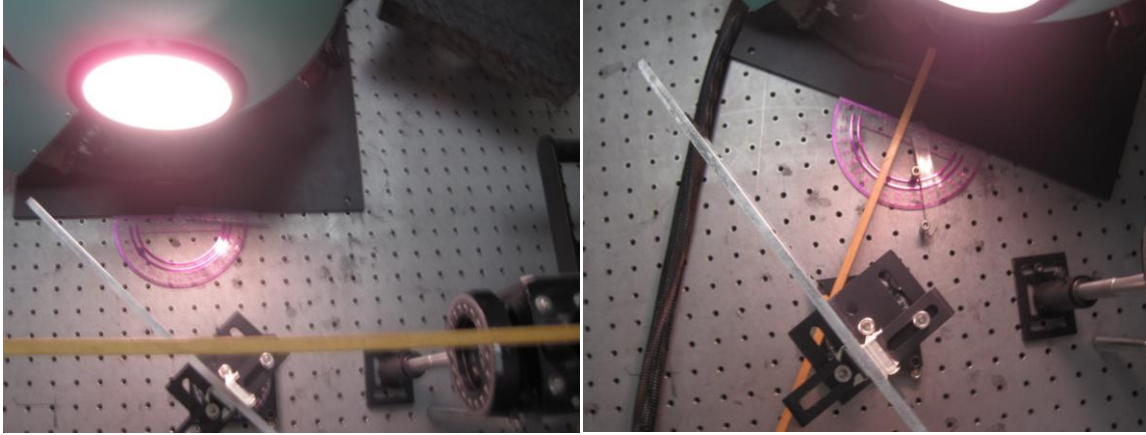
Figure 29. Alignment of the center of the integrating sphere with the intersection of aluminum and line of sight with the FTIR. Incident angle is 45 degrees.

Placement of the light source is also important to get the correct angle of incidence. To test if it is in the correct location, small rotations of the target will change the voltage detected. If the desired incident angle of the target is maximizes the signal, then the light source is in the correct position.   If a clockwise rotation increases the signal, the light source needs to be moved to the left relative to the surface normal to the target. If a counter-clockwise rotation increases the signal, the light source needs to be move to the right. Depending on distance, alignment errors of a centimeter can cause misalignments in incident angle of 2-4 degrees which can make for significant errors of DOLP measurements at larger incident angles.   This procedure is diagramed in figure 30.
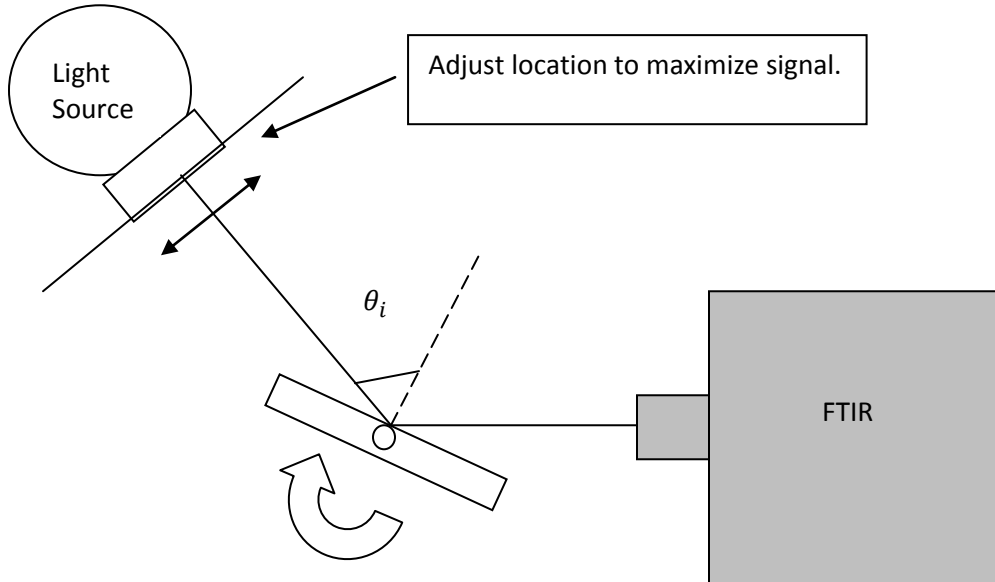
Figure 30. Alignment procedure for light source to ensure proper intersection with FTIR line of sight.

By following this alignment procedure, the error in incident angle alignment is estimated to be less than 2 degrees.

For each target angle, four spectropolarmetric measurements are made corresponding to polarizer positions of 0,45,90,135 degrees. These are recorded as interferograms which are converted to spectrum by taking the Fourier transform of the interferogram. These uncalibrated intensities represent the components that are combined to make the Stokes vectors. This data can be converted to be functions of wavelength in microns with the following conversion,

$$wavelength\ (\mu m) = \frac{10,000}{wavenumber(\ cm^{-1})}. \qquad (4\text{-}8)$$

Sample interferograms and spectrum emitted from the integrating sphere are included in figure 31.
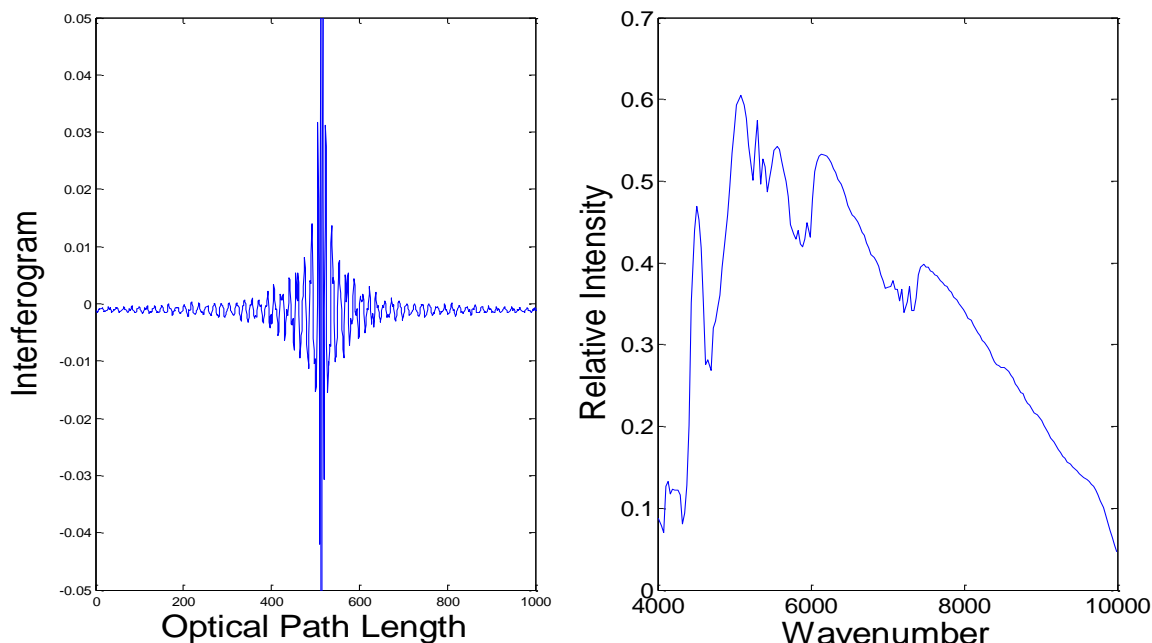
Figure 31. a) Sample interferogram from the Bomem 254 FTIR. b) Spectrum emitted from the integrating sphere produced after taking the Fourier transform of the interferogram.

To reduce the noise in the spectrum, the resolution for the spectrum is 64 wavenumbers cm^{-1}.

Aluminum Measurements

For smooth surfaces, Fresnel's equations describe how perpendicular and parallel components of the electric field are reflected. Using these equations and the measured complex index of refraction, the DOLP can be calculated for Aluminum for incident angles between zero and ninety degrees. Using the polarimetric biases measured in figure 23 and applying them to the uncalibrated measured spectra through equation (4-9) at a single wavelength for each incident angle produces data for the DOLP from an Aluminum target in figures 32.
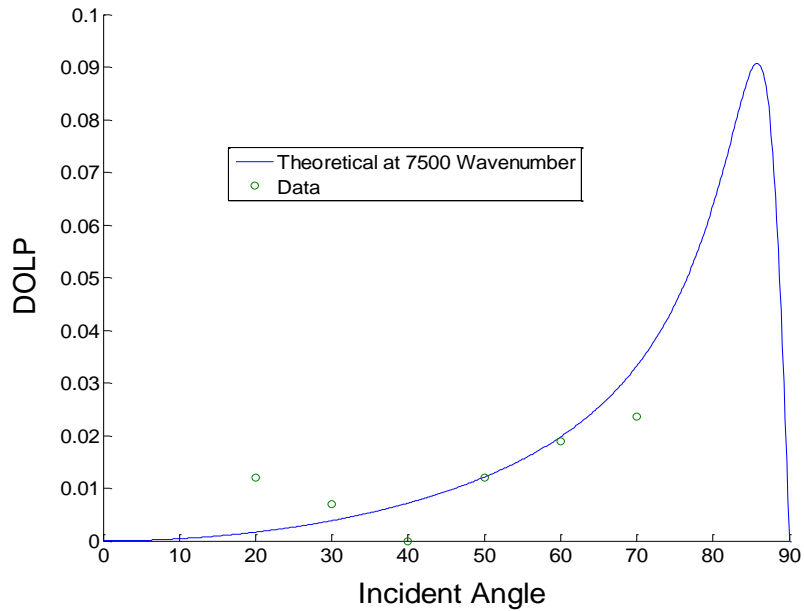
Figure 32. Measured values of reflected DOLP from a smooth aluminum surface versus target angle for the Bomem FTIR at 7500 wavenumbers. The theoretical curve is generated using Fresnel's equations and the complex index of refraction of pure Aluminum.

Due to the small difference between irradiances measured at 0 and 90 degrees of the polarizer orientation, there is a minimum measureable DOLP due to noise. Figure 32 shows this noise limit is approximately 1 percent.

Spectral DOLP of Aluminum

Using Fresnel's equations for a fixed incident angle and the complex index of refraction for aluminum, the DOLP reflected from Aluminum can be predicted for a smooth surface. Using the polarimetric biases and applying them to the uncalibrated spectra through equation (4-9) for the spectral range of the FTIR, excluding the wavelengths where instrument self emission is a problem, spectrally resolved DOLP measurements are produced. Figure 33 shows the uncalibrated spectra measured from Aluminum with an incident angle of 50 degrees. Figure 34 shows the calibrated spectra

for the raw data collected in figure 33 which shows the importance of correcting for the polarization bias of the FTIR.
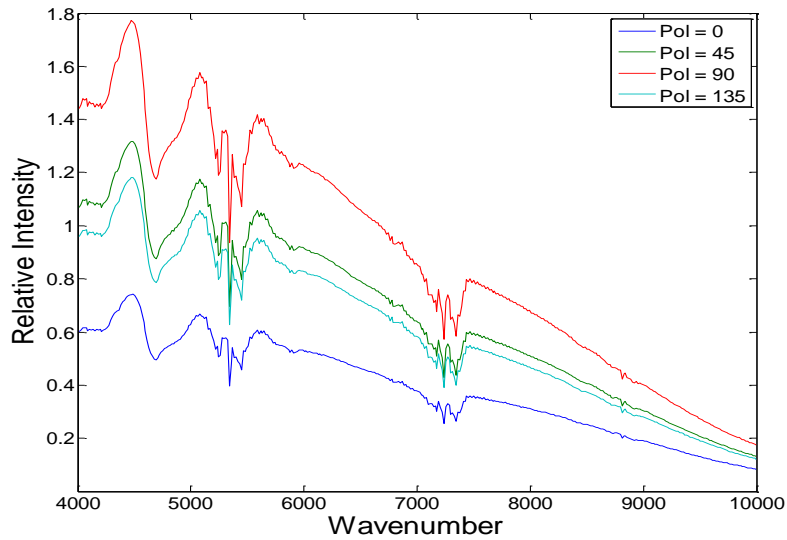
Figure 33. Uncalibrated spectrum collected from Aluminum at an incident angle of 50 degrees.
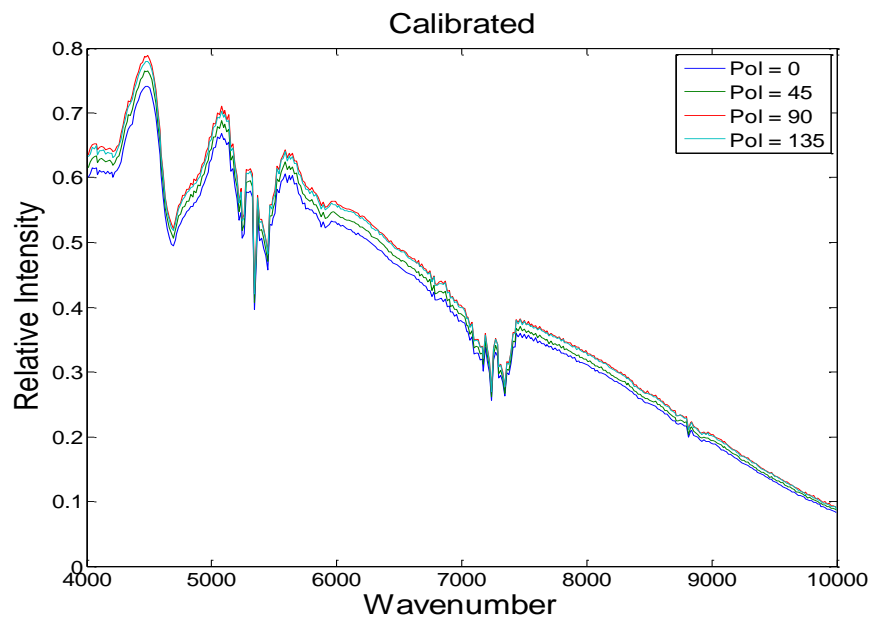
Figure 34. Calibrated spectrum collected from Aluminum at an incident angle of 50 degrees.

From the calibrated measurements in figure 34, Stokes parameters can be calculated using equations (4-4) through (4-7). Figure 35 shows the spectral dependence of the Stokes parameters.
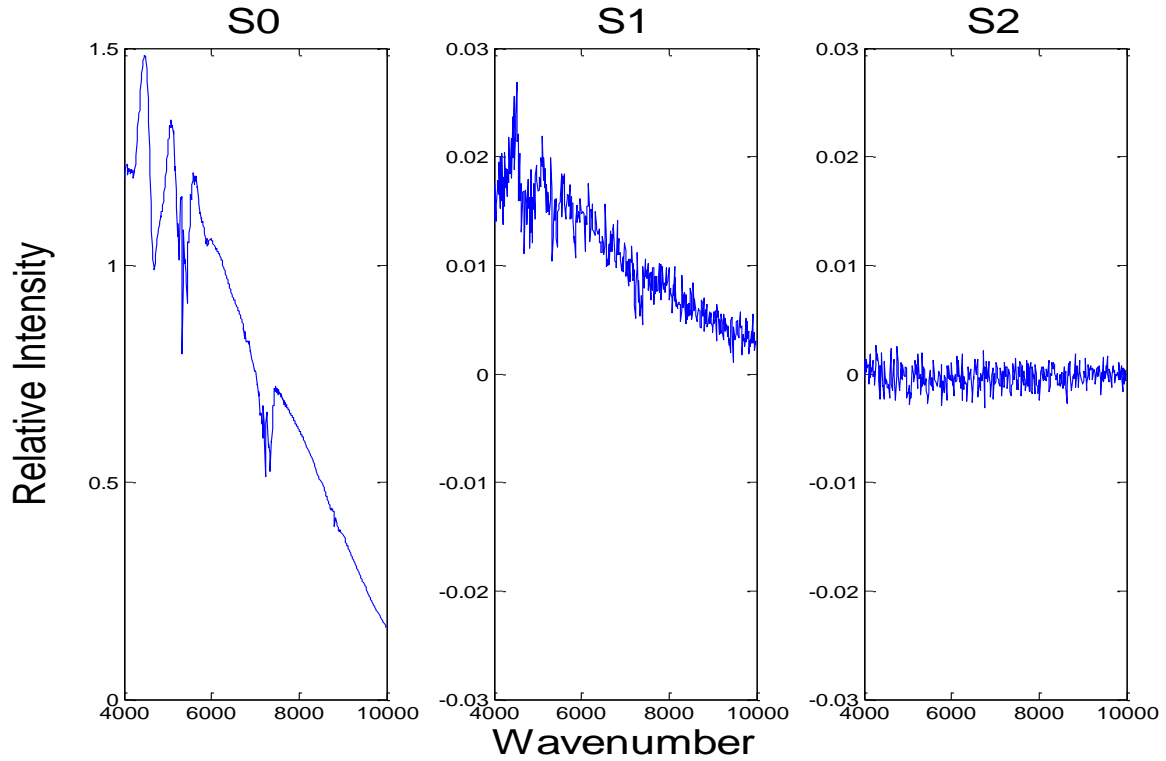
Figure 35. Stokes vectors for reflected spectrum at an incident angle of 50 degrees for aluminum.

Applying this sequence for all incidence angles measured, the DOLP can be spectrally resolved. Figure 36 shows the reflected DOLP from Aluminum for five incident angles.
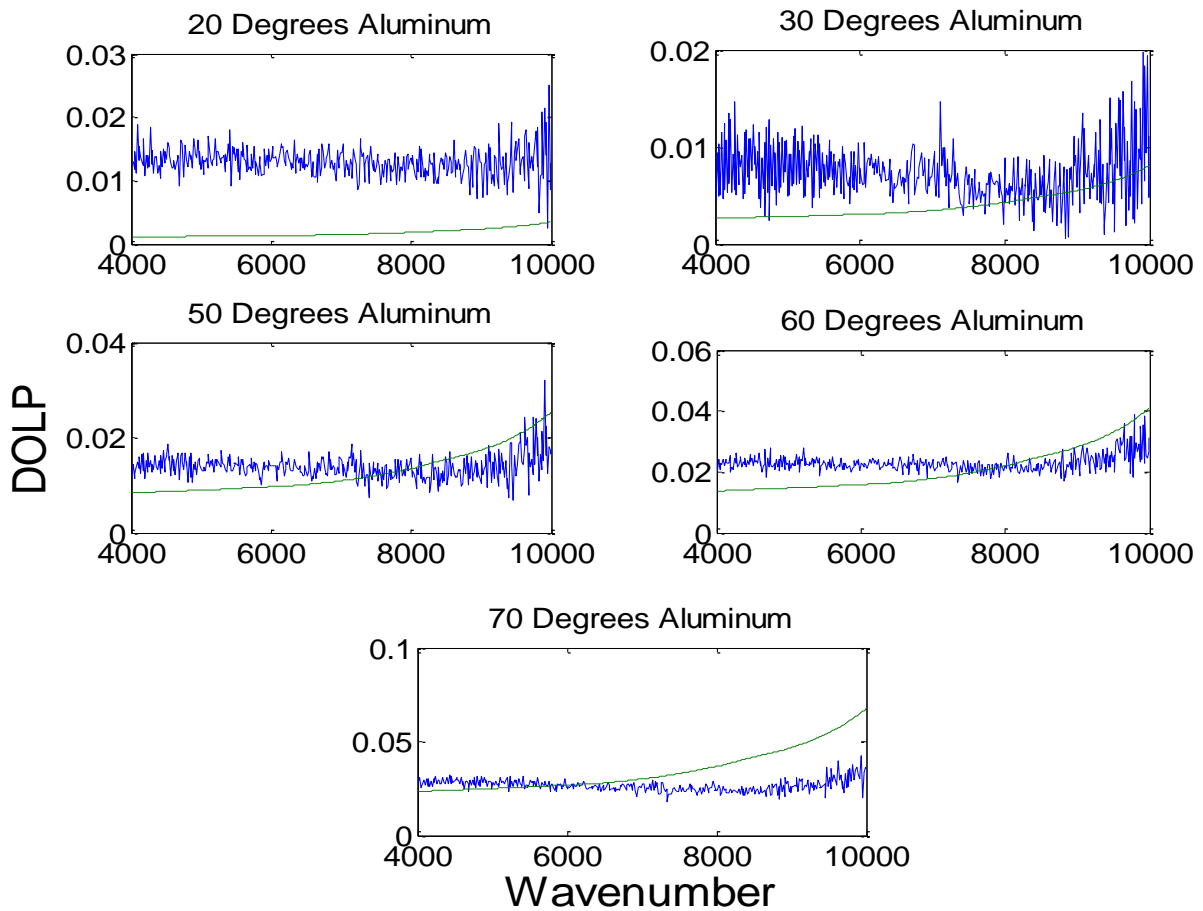
Figure 36. Measured and theoretical DOLP of smooth Aluminum for incidents angles of 20- 70 degrees. The blue line is the collected data and the green line is the theoretical DOLP based on Fresnel's equations.

The data collected does not follow the trend that theory predicts. Several factors were addressed to correct for the deviations. The wire grid polarizer extinction ratio is not known beyond 4000 wavenumbers. The measurements shown in figure 23 show how the polarimetric response of the FTIR trends toward one with increasing wavenumber. This indicates that the polarizer's performance is decreasing toward the near IR which inhibits the ability to compensate for the polarization bias of the FTIR beyond 4000 wavenumbers. Based upon this, the accuracy is best at 4000 wavenumbers and the amount of decrease in performance is unknown. This factor combined with the

calibration drift with instrument temperature limit the accuracy of the measurements collected.

Glass DOLP

Surface roughness decreases the DOLP of reflected and emitted radiation. Using the micro facet model and using a Gaussian distribution of slope values, the decrease in DOLP can be modeled as outlined in the previous chapter. By applying these principles, the effects of a rough surface can be seen on two samples of glass, one smooth, the other roughened by sandblasting. Thanks to the contribution from AFRL, the glass surfaces were measured with a scanning electron microscope (SEM) to determine the root mean squared (RMS) of the slopes. Results for the smooth are displayed in figures 37 and figures 38 & 39 are the results for the rough glass sample. The pictures on the left side of the figures are an image of the corresponding surface.

Roughness Measurement

	Whole Area
Total Area St.	2537.8271 µm²
Roughness A	5.3922 nm
Root mean sq	9.6396 nm
Ten Points He	271.1217 nm
Range Sr:	313.8280 nm

0µm   25.14µm   50.28µm
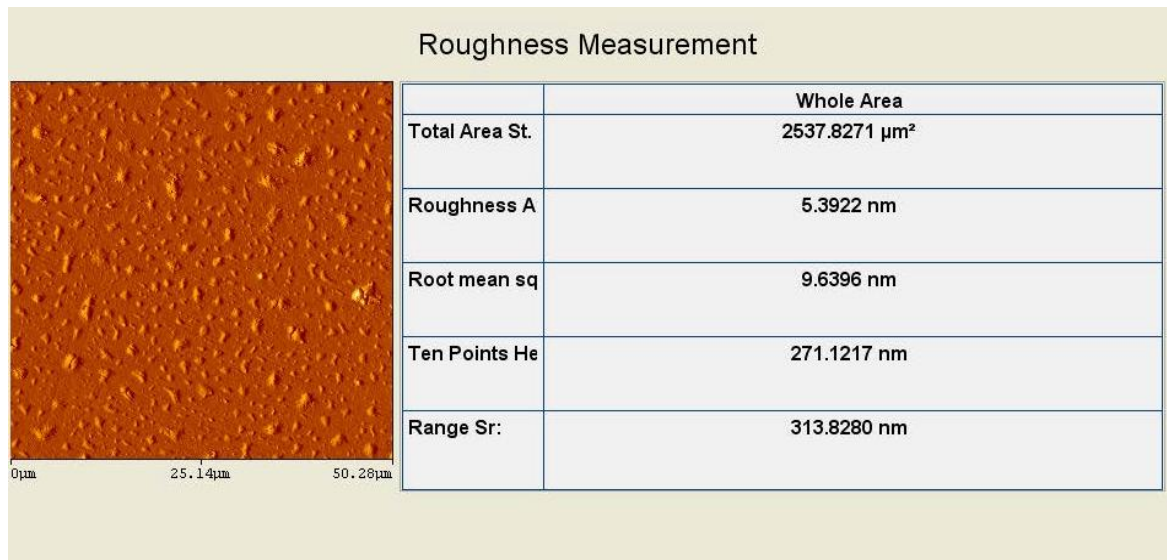
Figure 37. SEM picture of the smooth glass sample with RMS value showing a negligible surface roughness of 9 nm.

Roughness Measurement

	Whole Area
Total Area St.	5607.6895 μm²
Roughness A	533.1887 nm
Root mean sq	760.7017 nm
Ten Points He	5199.8667 nm
Range Sr:	5429.4595 nm
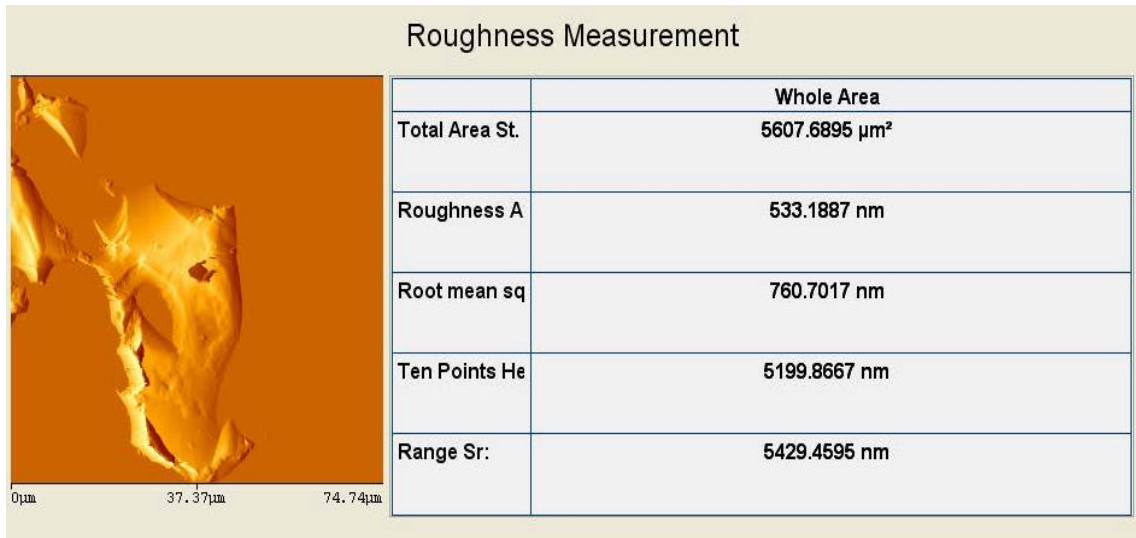
Figure 38. SEM picture of the rough glass sample with a RMS of value of 0.76 microns for the surface slopes.
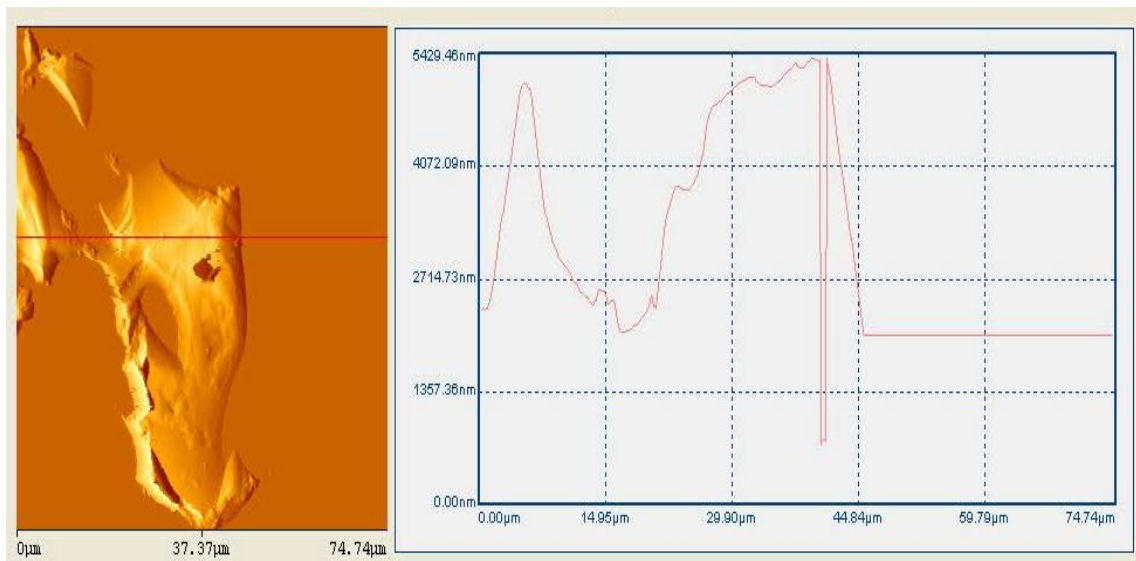
Figure 39. Line analysis showing the height of the surface roughness heights are up to 5 microns.

For these values of the RMS or, m_o from the previous chapter, the theoretical value of the DOLP versus incident angle is shown in figure 40.
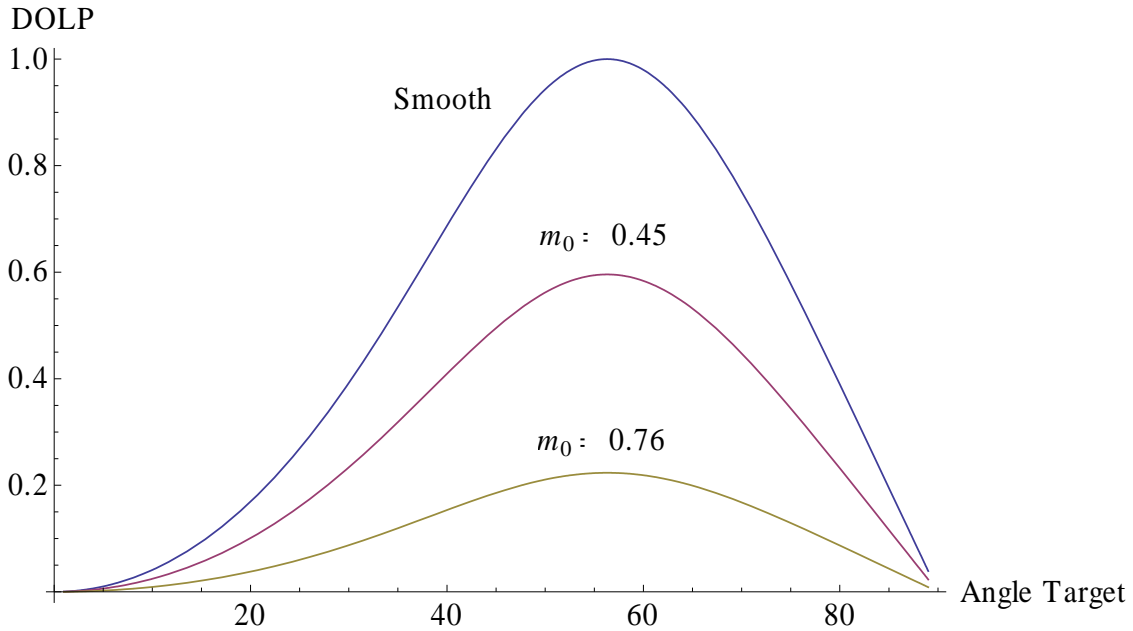
Figure 40. Reflected DOLP from Pyrex. These three curves indicate how the root mean square value of the surface roughness slope decreased the reflected DOLP as a function of angle.

By employing the same measurement procedures for the aluminum sample and the polarimetric calibration method, experimental results confirm that with the DOLP decreases with increases in surface roughness. This data is displayed below in figure 41, first for the smooth sample and in figure 42 for the rough sample. Due to the index of refraction not varying over the spectral range measured, the theoretical value stays constant spectrally; therefore only one theoretical plot is presented for at 5000 wavenumbers. Plotting three data points over the spectral range gives an indication of the noise in the measurement.
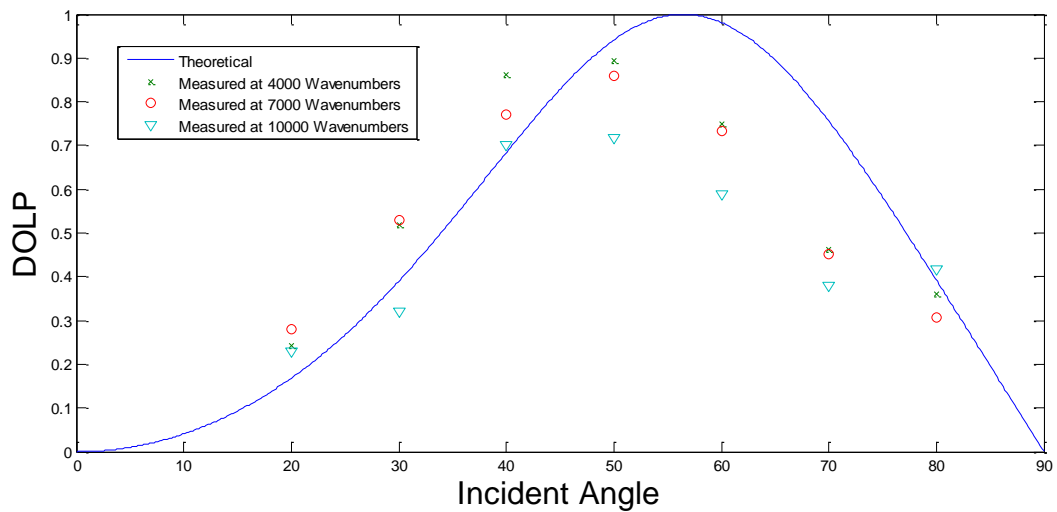
Figure 41. Showing the theoretical DOLP for smooth Pyrex for 5000 wavenumbers and measured DOLP versus target angle for three different wavenumbers.
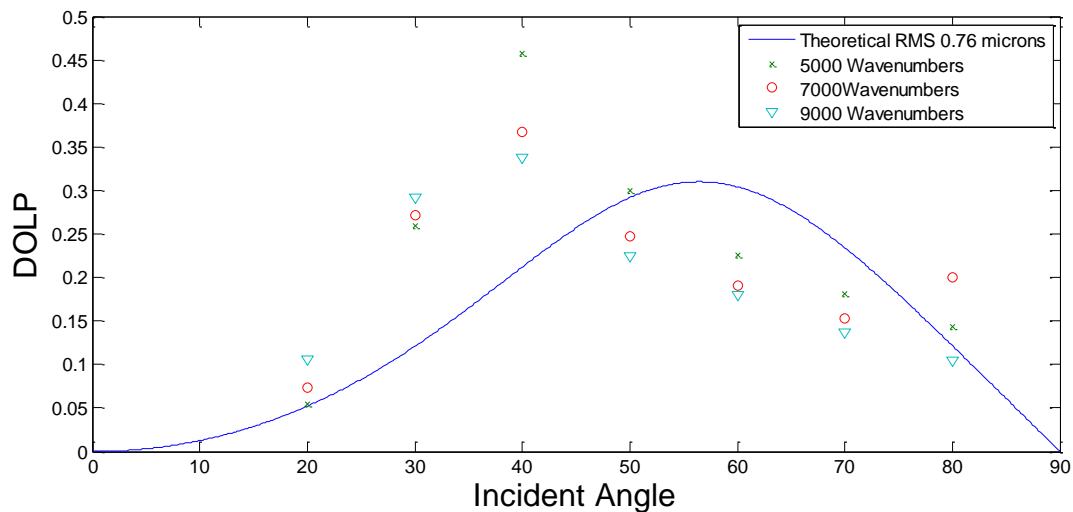
Figure 42.   Showing the theoretical DOLP for smooth Pyrex glass at 5000 wavenumbers and measured DOLP of rough glass with RMS slope of 0.76 versus target angle.

For the smooth glass, the general theoretical trend is measured.   However, significant deviations from theory are recorded at 50, 60, and 70 degrees. For the rough glass, significant deviations from predicted values are measured without a clear trend. One challenge presented with the samples chosen was their size.   Only being five

centimeters long made measurements difficult at the larger incident angles which increased noise. Also, the possibility of reflections from the material used to hold the glass in place could have contributed to the errors. The rough glass sample reflected light is a diffuse manner, limiting the amount of light that could be collected. As a result, the differences in the Stokes parameters measured were small. When the first parameter is artificially low due to the low signal, spikes in the measured DOLP are recorded. This can be seen at incident angles of 30 and 40 degrees. Figures 43 and 44 show the spectrally resolved DOLP measurements for the smooth and rough glass.

Spectral DOLP of Smooth and Rough Glass
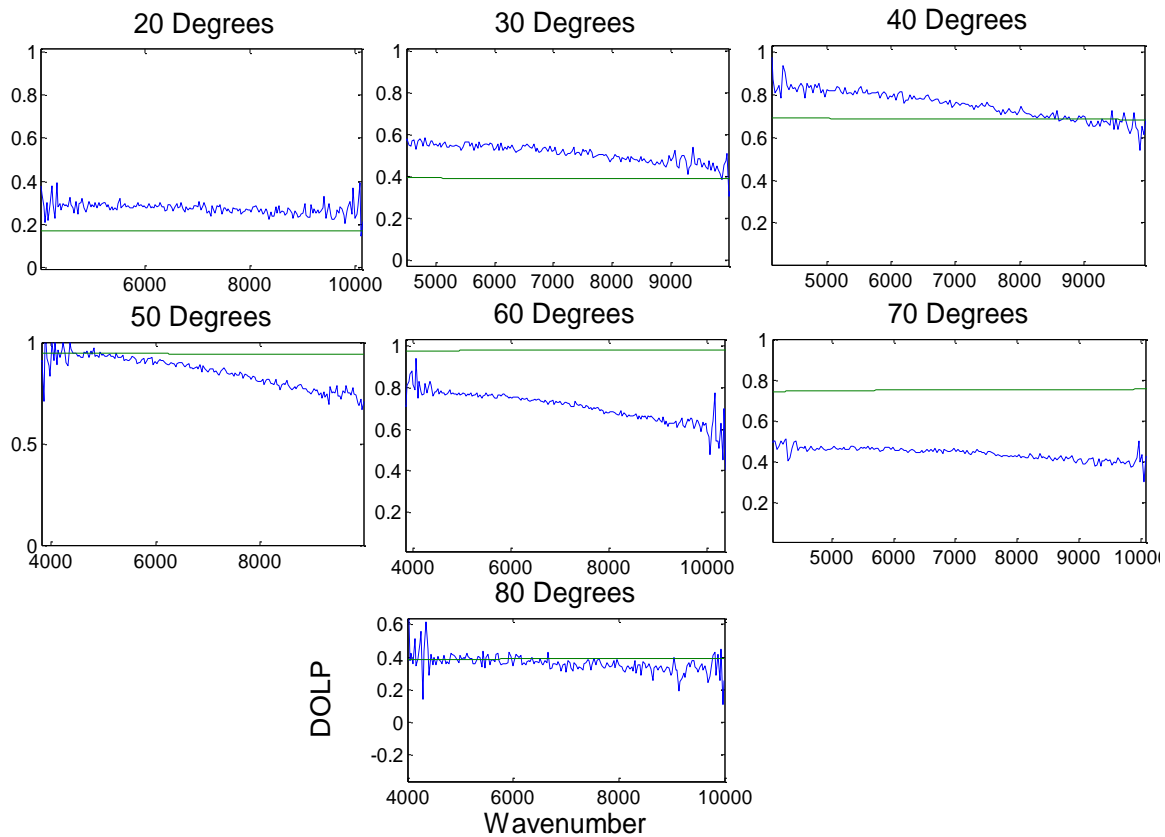
Figure 43. Smooth Glass DOLP for incident angles of 20-80 degrees
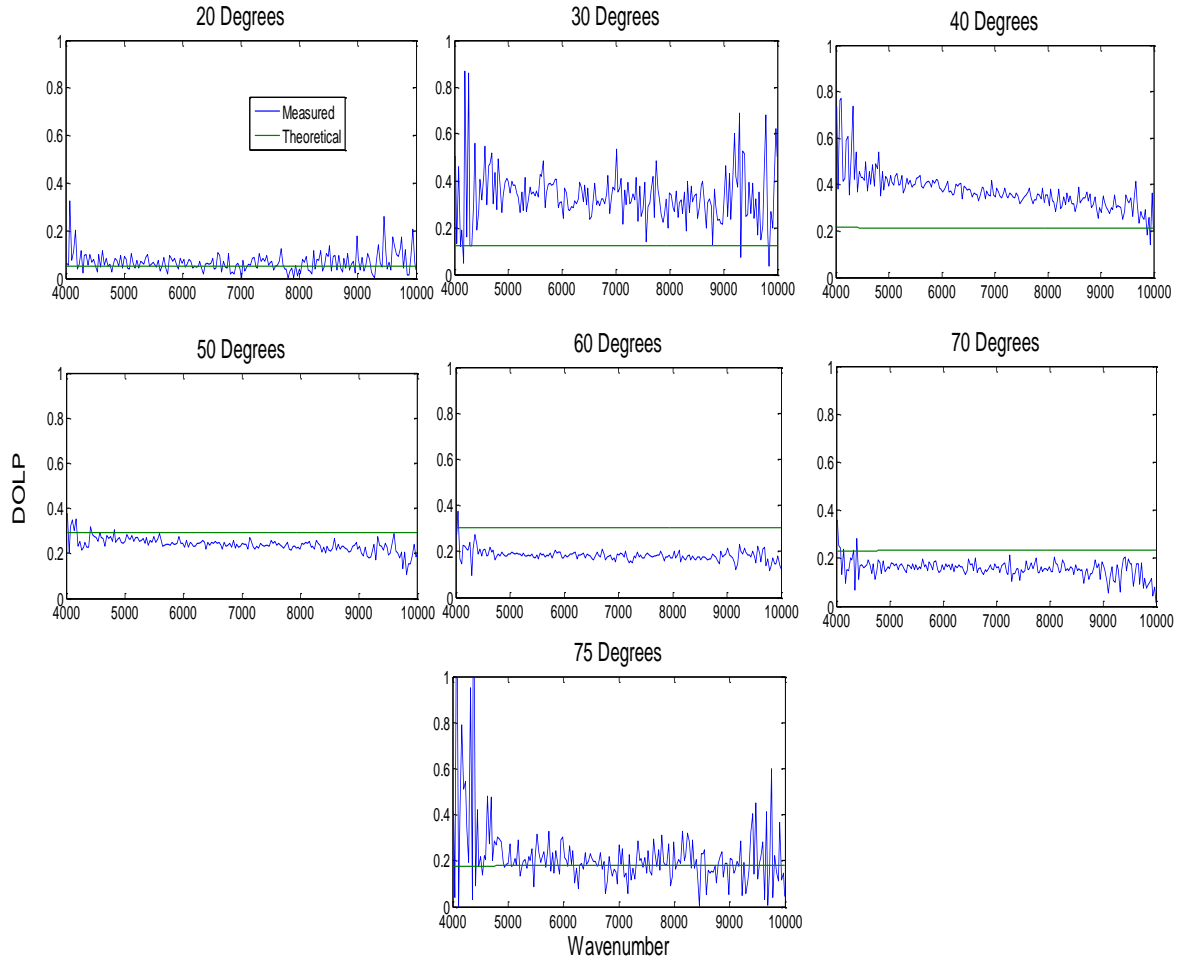
Figure 44. Measured DOLP from roughened glass sample for incident angles of 20-75 degrees. Theoretical curves use the measured RMS value of 0.76.

Experimental results for the smooth glass sample agree poorly with the theoretically predicted values based on Fresnel's equations while the results for the roughened glass agree better for a few incident angles. The decreasing slope in the measured spectrum shown strongly at 40, 50, and 60 degrees for smooth glass, indicates the decreasing performance of the wire-grid polarizer. However, the output of the light source used emitted strongly in the longer wavelengths but decreased significantly toward the NIR increasing the noise. This factor, combined with the small cross section of material that can reflect light at larger incident angles also increase the noise.

V. Conclusions

Fourier transform spectrometry has allowed for numerous spectral phenomena to be investigated. The ability to simply place a polarizer in front of an FTIR to enable spectropolarimetric measurements allows additional information to be collected. Spectrally resolved polarimetric phenomena allows for the potential of broad application in remote sensing.

The scope of this work was threefold: (1) to establish a new, spectro-polarimetric reflectance measurement capability at AFIT; (2) document best practices (learned through this effort) for accurate DOLP measurements; (3) demonstrate the current accuracy and limitations of the technique using smooth aluminum as well as smooth and roughened glass substrates. These goals were accomplished to varying degrees of success. Based on the results of the experiments conducted, numerous challenges were uncovered that were not obvious at the beginning. For example, the stability of the polarization bias was assumed to be temperature independent which was shown to be a faulty assumption. Also, the performance of the polarizer was shown to be important to accurate polarimetric calibrations. A technique for alignment of the light source and target sample was successful produced to achieve small error of incident angle. This procedure can be applied to future work. However, a mechanically controlled process would yield more accurate results. The combination of these factors inhibited consistent results from being produced, limiting the confidence of the accuracy achieved. Based on the challenges addressed, a firm understanding of the instrumental limitation can be avoided on future experiments.

Several important considerations for future work were uncover through these experiments. Having precisely known materials to measure is critical to compare with theory because Fresnel's equations are strong functions of the index of refraction associate with the material. Also, careful characterization of the surface parameters is important for determining the affect they have on the DOLP. In addition, the impact of having an oxidized surface impacts the DOLP. Having well characterized samples will be important for determining the ultimate accuracy of this method. Although the measured results for the Aluminum and glass samples did not match theory well, the general trend and magnitude of the reflected DOLP was shown. Based on these initial measurement and the challenges uncovered, the accuracy of future measurements can be vastly improved.

Suggestion for future work

In order to utilize the unique advantages of the FTIR, materials other than glass and aluminum should be studied. Due to the material's largely flat refractive indices in the spectral range studied, no spectral features are readily available to measure. To incorporate a strong spectral signature, adding additional layers to known, pure materials, would be of interest. This could be achieved by simply adding a layer of water to the materials investigated [19, 22, 23]. This would also extend the multiple layer model highlighted in the previous chapter.

Possible areas for future related research are numerous. For example, the RMS of the surface slopes in the model is a characteristic of the material and does not depend upon the incident wavelength of light. When the wavelength is short compared to the

average surface roughness the reflection will tend to be diffuse having a depolarizing effect, therefore reducing the reflected or emitted DOLP. However, when the wavelength of light is long compared to the mean surface roughness, the surface effectively becomes smoother, and therefore increasing the amount of reflected or emitted polarized light resulting in a high DOLP. Evidence for this could be seen by comparing measured DOLP at a fixed incident angle for different wavelengths and for a fixed surface roughness. Fresnel's equations predict the amount of polarized light being reflected or emitted from a smooth surface. Comparing the DOLP at increasing wavelengths to the ideally smooth surface shows that there is a spectral dependence to the DOLP.

Other areas that could be investigated that would be ideally suited the spectropolarimetric imaging capabilities available at AFIT would be target detection. Also, using this capability to generate three dimensional information would prove useful in an operational setting [18]. Numerous other applications can be explored showcasing the incredible value that combining polarimetric and spectral information can provide.

Appendix A. Applicable MATLAB Code

[MATLAB CODE for theoretical DOLP]

```
index = xlsread('Aluminum Indices.xls');

ALn = index(:,2); % real
ALk = index(:,3); %imaginary
L = index(:,1); %wavelength

%interpolated function
nn = @(lambda) interp1(L,ALn,lambda);
kk = @(lambda) interp1(L,ALk,lambda);


% Fresnels equations

thp  = @(ni,nt,th) asin( real(ni./nt) .* sin(th) );
r_pe = @(th,ni,nt) ( ni.*cos(th) - nt.*cos(thp(ni,nt,th)) ) ./ (
ni.*cos(th)          + nt.*cos(thp(ni,nt,th)) );
r_pa = @(th,ni,nt) ( nt.*cos(th) - ni.*cos(thp(ni,nt,th)) ) ./ (
ni.*cos(thp(ni,nt,th)) + nt.*cos(th) );
R_pe = @(th,ni,nt) r_pe(th,ni,nt).*conj(r_pe(th,ni,nt));
R_pa = @(th,ni,nt) r_pa(th,ni,nt).*conj(r_pa(th,ni,nt));
DOLP = @(th,ni,nt) (R_pe(th,ni,nt)-
R_pa(th,ni,nt))./(R_pe(th,ni,nt)+R_pa(th,ni,nt));


%Dispersion relationship for the refractive index for glass

nn = @(lambda) sqrt(1 + (1.039*lambda.^2)/(lambda.^2 - 0.00600069867)+
0.231792344*lambda.^2/(lambda.^2 - 0.0200179144) +
1.01046945*lambda.^2/(lambda.^2 - 103.560653));
```

[MATLAB CODE for interpreting data]

```
% Import Data
f61 = 'AL80P0.I0B';
T61 = 200+273.15; % [K]
[y61,t61,Hdr61,Dr61] = importBomem154(f61);
[~,G80P0] = int2spec(y61,'Xmin',xm,'Xmax',xi,'apod','hann','PC',true);


Y    = real([G80P0; G80P45; G80P90; G80P135;] ./ PP);

%Stokes vectors
S0 = @(Y) Y(1,xi) + Y(3,xi);
S1 = @(Y) Y(3,xi) - Y(1,xi);
S2 = @(Y) Y(4,xi) - Y(2,xi);
S3 = @(Y) 0;

PP   = [ones(size(R0)); R45./R0; R90./R0; R135./R0;];
```

```
DOLP = sqrt(S1(Y).^2 + S2(Y).^2 + S3(Y).^2)./S0(Y)
```

[MATLAB CODE for thin surface]

```
index = xlsread('AL2O3.xls');


An = index(:,2); % real index
L = index(:,1); %wavelength

%interpolated function
n2 = @(lambda) interp1(L,An,lambda);


l = linspace(0.4,2.4,500);
xx = 10000./l;


th_d = 40; th = pi*th_d/180;


ni = 1; %index of air
nt = @(lambda) n2(lambda);


thp  = @(ni,nt,th)  asin( real(ni./nt) .* sin(th) ); %thp is in
radians


r_pe1 = @(th,ni,nt) ( ni.*cos(th) - nt.*cos(thp(ni,nt,th)) ) ./
( ni.*cos(th)+ nt.*cos(thp(ni,nt,th)) );


r_pa1 = @(th,ni,nt) ( nt.*cos(th) - ni.*cos(thp(ni,nt,th)) ) ./
( ni.*cos(thp(ni,nt,th)) + nt.*cos(th) );


R_pe1 = @(th,ni,nt)   r_pe1(th,ni,nt).*conj(r_pe1(th,ni,nt));
R_pa1 = @(th,ni,nt)   r_pa1(th,ni,nt).*conj(r_pa1(th,ni,nt));


T_pe = @(th,ni,nt) 1-R_pe1(th,ni,nt);
T_pa = @(th,ni,nt) 1-R_pa1(th,ni,nt);


%Aluminum Data

index2 = xlsread('Aluminum Indices.xls');


ALn = index2(:,2); % real
ALk = index2(:,3); %imaginary
LL = index2(:,1); %wavelength


%interpolated function
n3 = @(lambda) interp1(LL,ALn,lambda);
k3 = @(lambda) interp1(LL,ALk,lambda);


nt2 = @(lambda) n3(lambda);


%thp is the incident angle for reflection from the bottom layer
thp2  = @(nt2,ni,nt,th) asin( real(nt./nt2) .* sin(thp(ni,nt,th)) );
```

```
th_d2 = @(ni,nt,th) 180*thp(ni,nt,th)/pi;

r_pe2 = @(nt2,ni,nt,th) ( nt.*cos(thp(ni,nt,th)) -
nt2.*cos(thp2(nt2,ni,nt,th)) ) ./ ( nt.*cos(thp(ni,nt,th))        +
nt2.*cos(thp2(nt2,ni,nt,th)) )

r_pa2 = @(nt2,ni,nt,th) ( nt2.*cos(thp(ni,nt,th)) -
nt.*cos(thp2(nt2,ni,nt,th)) ) ./ ( nt.*cos(thp2(nt2,ni,nt,th)) +
nt2.*cos(thp(ni,nt,th)) );

R_pe2 = @(nt2,ni,nt,th)
r_pe2(nt2,ni,nt,th).*conj(r_pe2(nt2,ni,nt,th)).*T_pe(th,ni,nt);

R_pa2 = @(nt2,ni,nt,th)
r_pa2(nt2,ni,nt,th).*conj(r_pa2(nt2,ni,nt,th)).*T_pa(th,ni,nt);

RT_pe = @(th,ni,nt,thp,nt2) R_pe1(th,ni,nt)+R_pe2(nt2,ni,nt,th);
RT_pa = @(th,ni,nt,thp,nt2) R_pa1(th,ni,nt)+R_pa2(nt2,ni,nt,th);

DOLP = @(th,ni,nt,thp,nt2) (RT_pe(th,ni,nt,thp,nt2)-
RT_pa(th,ni,nt,thp,nt2))./(RT_pe(th,ni,nt,thp,nt2)+RT_pa(th,ni,nt,thp,n
t2));
```

Appendix B. FLIR imager DOLP measurements

In addition to the FTIR measurements, data was collect for glass using an infrared camera. The spectral response of the FLIR imager is in the NIR. By taking these measurements with this camera and not placing a dark background behind the transparent glass samples, EM radiation that was transmitted through the sample is detectable by the imager. Since, most light is unpolarized, this had the effect of lowering the measured DOLP at all incident angles. Also, the polarizer used is not designed for the spectral response of the camera effectively lowering the amount of polarization difference that can be detected. Figures 45 through 47 show the results of the measurements taken.
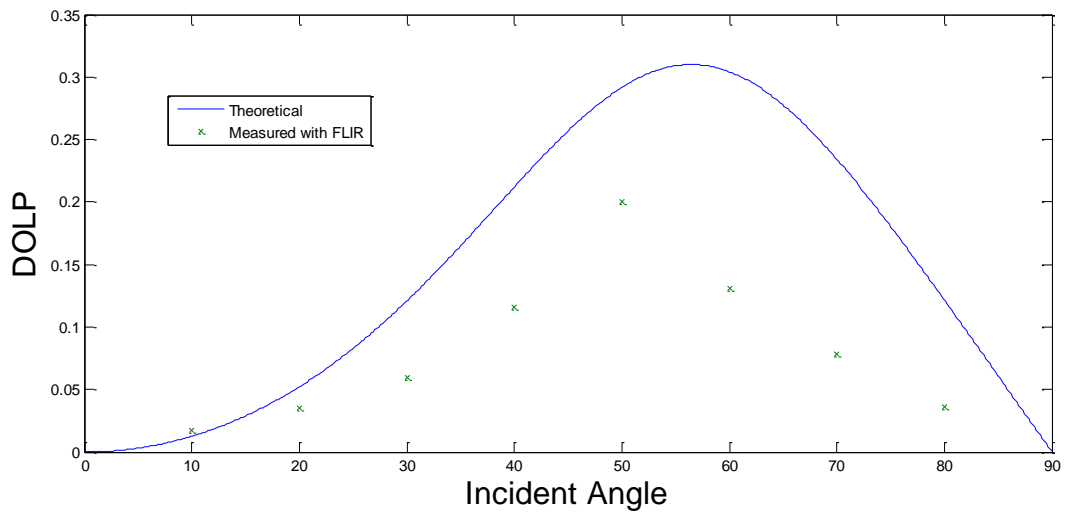
Figure 45. DOLP vs incident angle for rough glass RMS value 0.76 microns measured with the FLIR imager.

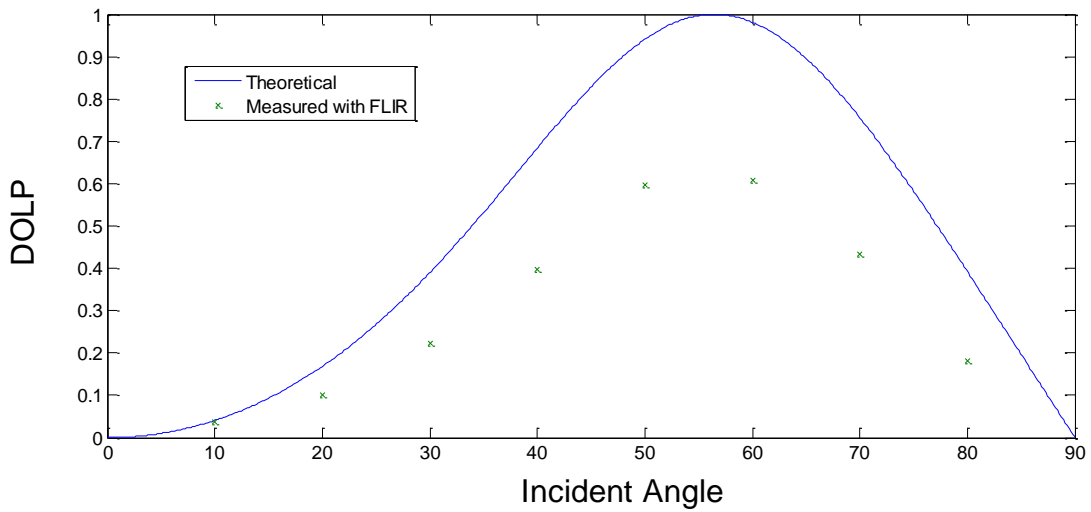**Figure 46. DOLP vs incident angle for smooth glass RMS value 0.09 microns measured with the FLIR imager.**
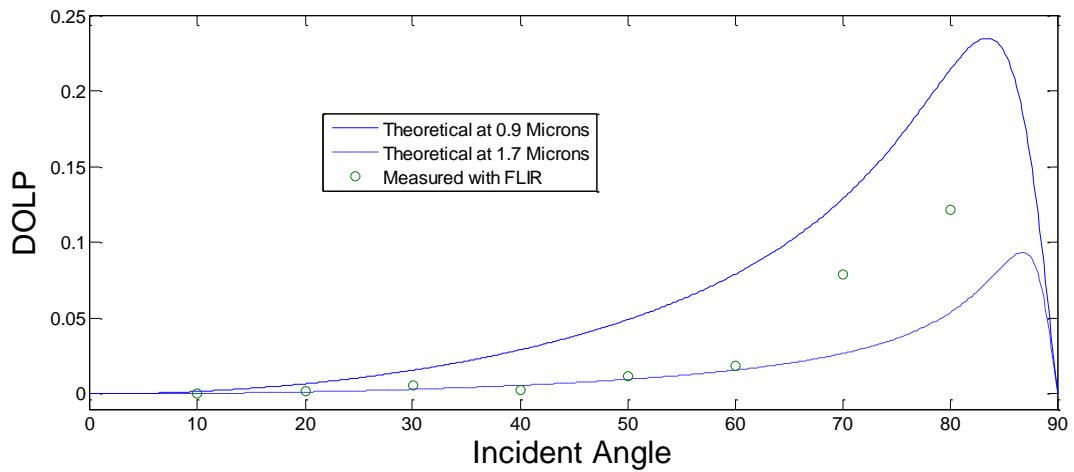

Figure 47.   Measured values of reflected DOLP from smooth aluminum versus target angle for the FLIR imager. The two theoretical curves correspond to the limits of the spectral response of the imager, 0.9 and 1.7 microns.

Bibliography

[1]   Hecht, Eugene. Optics. Addison Wesley, 1301 Sansome St., San Francisco, CA 94111, 2002. ISBN 0-8053-8566-5.

[2]   D. L. Jordan and G. Lewis, "Measurement of the effect of surface roughness on the polarization state of thermally emitted radiation," Opt. Lett. **19**, 692-694 (1994).

[3]   D. Jordan, G. Lewis, and E. Jakeman, "Emission polarization of roughened glass and aluminum surfaces," Appl. Opt. 35, 3583-3590 (1996).

[4]   James R. Shell. *Bidirectional Reflectance: An overview with Remote Sensing Applications and Measurement Recommendations.* SPIE, 2004.

[5]   Kristan P. Gurton, Rachid Dahmani. *Effect of surface roughness and complex indices of refraction on polarized thermal emission.* Applied Optics, 2005 Vol 44, No. 25.

[6]   J. Tyo, D. Goldstein, D. Chenault, and J. Shaw, "Polarization in Remote Sensing--introduction," Appl. Opt. 45, 5451-5452 (2006).

[7]   J. Tyo, D. Goldstein, D. Chenault, and J. Shaw, "Review of passive imaging polarimetry for remote sensing applications," Appl. Opt. 45, 5453-5469 (2006).

[8]   D. B. Chenault, "Infrared Spectropolarimetry," Ph.D. dissertation. University of Alabama in Huntsville, 1992.

[9]   M. Eismann, "Hyperspectral Remote Sensing", course notes for a graduate level class, 2006.

[10]   Christopher M. Persons ; Michael W. Jones ; Craig A. Farlow ; L. Denise Morell ; Michael G. Gulley ; Kevin D. Spradley; A proposed standard method for polarimetric calibration and calibration verification. Proc. SPIE 6682, Polarization Science and Remote Sensing III, 66820K (September 13, 2007); doi:10.1117/12.732137.

[11]   O. Sandus, "A Review of Emission Polarization," Appl. Opt. 4, 1634-1642 (1965).

[12]   Shaw, "Degree of Linear Polarization in Spectral Radiances from Water-Viewing Infrared Radiometers," Appl. Opt. 38, 3157-3165 (1999).

[13]   F. Nicodemus, "Reflectance Nomenclature and Directional Reflectance and Emissivity,"   Appl. Opt. 9, 1474-1475 (1970).

[14]   David B. Chenault ; J. Larry Pezzaniti ; Russell A. Chipman; Mueller matrix algorithms. Proc. SPIE 1746, Polarization Analysis and Measurement, 231 (December 11, 1992); doi:10.1117/12.138793.

[15]   J. R. Schott, *Fundamentals of Polarimetric Remote Sensing*, Vol. TT81, *SPIE Tutorial Texts In Optical Engineering* (2009).

[16]   M. Eismann, "Hyperspectral Remote Sensing", course notes for a graduate level class, 2006

[17]   2. D. H. Goldstein, R. A. Chipman, and D. B. Chenault Infrared, "Spectropolarimetry," *Opt. Eng.* 28 (2), pp. 120-125,1989.

[18]   M. Vedel ; N. Lechocinski ; S. Breugnot; 3D shape reconstruction of optical element using polarization. Proc. SPIE 7672, Polarization: Measurement, Analysis, and Remote Sensing IX, 767203 (April 23, 2010); doi:10.1117/12.850780.

[19]   G. Hale and M. Querry, "Optical Constants of Water in the 200-nm to 200-µm Wavelength Region," Appl. Opt. 12, 555-563 (1973).

[20]   Dennis H. Goldstein ; Joseph L. Cox; Spectropolarimetric properties of vegetation. Proc. SPIE 5432, Polarization: Measurement, Analysis, and Remote Sensing VI, 53 (July 15, 2004); doi:10.1117/12.546808.

[21]   Kristan P. Gurton ; Melvin Felton; Detection of disturbed earth using passive LWIR polarimetric imaging. Proc. SPIE 7461, Polarization Science and Remote Sensing IV, 746115 (August 11, 2009); doi:10.1117/12.837779.

[22]   J. Shaw, "Polarimetric Measurements of Long-Wave Infrared Spectral Radiance from Water," Appl. Opt. 40, 5985-5990 (2001).

[23]   J. Shaw, "Degree of Linear Polarization in Spectral Radiances from Water-Viewing Infrared Radiometers," Appl. Opt. 38, 3157-3165 (1999).

[24]   Jason P. Meyers ; John R. Schott ; Scott D. Brown; Incorporation of polarization into the DIRSIG synthetic image generation model. Proc. SPIE 4816, Imaging Spectrometry VIII, 132 (November 1, 2002); doi:10.1117/12.451545.

[25]   R. G. Priest and T. A. Germer, "Polarimetric BRDF in the microfacet model: Theory and measurements,"*Proceedings of the 2000 Meeting of the Military Sensing Symposia Specialty Group on Passive Sensors* **1**,pp. 169–181, 2002.

[26]   Richard A. Anderson; Polarized properties of the directional-hemispherical reflectance and emissivity of an opaque surface. Proc. SPIE 1747, Polarization and Remote Sensing, 49 (December 8, 1992); doi:10.1117/12.138830.

[27]   "Refractive Index Database", September 2012. URL http://refractiveindex.info/.

[28]   Why scatter can polarize light. J. Alcoz. 3 September 2012 <http://www.polarization.com>.

[29]   H.E. Scott, S.H. Jones, F. Iannarilli, K. Annen, "Hyperspectral IR polarimetry with application in demining and unexploded ordnance detection," SPIE Vol. 3534 (1998).

[30]   Pesses, M., Tan, J., Hash, R., & Swartz, R. (2002). "Simulation of LWIR polari-metric observations of space objects." IEEE Computer Society Proceedings of the 31st Applied Imagery Pattern Recognition Workshop, pp. 164–170.

[31]   Rosario, D.S.; , "Highly effective logistic regression model for signal (anomaly) detection," *Acoustics, Speech, and Signal Processing, 2004. Proceedings. (ICASSP '04). IEEE International Conference on* , vol.5, no., pp. V- 817-20 vol.5, 17-21 May 2004 doi: 10.1109/ICASSP.2004.1327236

[32]   João M. Romano ; Dalton Rosario; Random sampling statistical analysis for adaptive target-scale-invariant hyperspectral anomaly detection. Proc. SPIE 6565, Algorithms and Technologies for Multispectral, Hyperspectral, and Ultraspectral Imagery XIII, 656522 (May 07, 2007); doi:10.1117/12.719082.

[33]   Chabitha Devaraj ; Scott Brown ; David Messinger ; Adam Goodenough ; David Pogorzala; A framework for polarized radiance signature prediction for natural scenes. Proc. SPIE 6565, Algorithms and Technologies for Multispectral, Hyperspectral, and Ultraspectral Imagery XIII, 65650Y (May 07, 2007); doi:10.1117/12.719798.

[34]   Shell, James, "Polarimetric Remote Sensing in the Visible to Near Infrared," Ph. D. dissertation. Rochester Institute of Technology, 2005.

[35]   Joao M. Romanoa, Melvin Feltonb, David Chenault, Brian Sohrd, Proc. of SPIE Vol. 7696 769611-1 doi: 10.1117/12.849911.

[36]   Michael W. Kudenov, J. Larry Pezzaniti, Grant R. Gerhart. Microbolometer-infrared imaging Stokes polarimeter. Optical Engineering 48_6_, 063201 _June 2009.

[37]   Bradley, Kenneth C., Kevin C. Gross, and Glen P. Perram. "Remote identification and quantification of industrial smokestack effluents via imaging
Fouriertransform
spectroscopy". Environmental Science and Technology, NA:NA, 2010.*Environ. Sci. Technol.* **2010.**

[38]   L.P.H. Jeurgens, W.G. Sloof, F.D. Tichelaar, C.G. Borsboom, E.J. Mittemeijer. "Determination of thickness and composition of aluminium-oxide overlayers on aluminium substrates."Applied Surface Science 144–145 _1999. 11–15.

REPORT DOCUMENTATION PAGE

Form Approved
OMB No. 074-0188

1. REPORT DATE *(DD-MM-YYYY)* 21 March 2013	2. REPORT TYPE Master's Thesis	3. DATES COVERED *(From – To)* Aug 2011 – Mar 2013

4. TITLE AND SUBTITLE Development of a Spectropolarimetric Capability	5a. CONTRACT NUMBER
	5b. GRANT NUMBER
	5c. PROGRAM ELEMENT NUMBER
6. AUTHOR(S) Carlson, Evan J. Captain, USAF	5d. PROJECT NUMBER
	5e. TASK NUMBER
	5f. WORK UNIT NUMBER

7. PERFORMING ORGANIZATION NAMES(S) AND ADDRESS(S) Air Force Institute of Technology Graduate School of Engineering and Management (AFIT/EN) 2950 Hobson Way, Building 640 WPAFB OH 45433	8. PERFORMING ORGANIZATION REPORT NUMBER AFIT-ENP-13-M-05

9. SPONSORING/MONITORING AGENCY NAME(S) AND ADDRESS(ES) Dave Petersen Defense Threat Reduction Agency 8725 John J. Kingman Road Fort Belvoir, VA 22060	10. SPONSOR/MONITOR'S ACRONYM(S) DTRA
	11. SPONSOR/MONITOR'S REPORT NUMBER(S) 2437-M (Polarimetric HSI)

12. DISTRIBUTION/AVAILABILITY STATEMENT
Distribution STATEMENT A: APPROVED FOR PUBLIC RELEASE; DISTRIBUTION UNLIMITED

13. SUPPLEMENTARY NOTES

This material is declared a work of the U.S. Government and is not subject to copyright protection in the United States.

14. ABSTRACT

A Bomem 200 series Fourier transform infrared spectrometer and FLIR Systems Inc InGaAs infrared (IR) camera was used to measure the degree of linear polarization (DOLP) from a metal and glass surfaces. This was accomplished by placing a wire grid polarizer in front of the aperture of the FTIR and IR camera to measure the polarized reflection from the target material. For the IR camera, an average of pixel counts was collected over the area of the target to measure to DOLP. Factors impacting the accuracy of the measurements from the FTIR are calibration, instrument self emission, and alignment error. Factors impacting the value of the DOLP from the material are the complex index of refraction, angle of incidence, and surface roughness. Results of these measurements match theory with varying success and also show the limitation and challenges associated with the physical limitation of the equipment used.

15. SUBJECT TERMS
Polarimetry, Fourier Transform Spectrometer, DOLP, Spectropolarimetry, Stokes

16. SECURITY CLASSIFICATION OF:			17. LIMITATION OF ABSTRACT	18. NUMBER OF PAGES	19a. NAME OF RESPONSIBLE PERSON Dr. Kevin C. Gross, AFIT/ENP
a. REPORT U	b. ABSTRACT U	c. THIS PAGE U	UU	92	19b. TELEPHONE NUMBER *(Include area code)* (937) 255-3636, x 4558 (Kevin.gross@afit.edu)

Standard Form 298 (Rev. 8-98)
Prescribed by ANSI Std. Z39-18